8-9-2014

GEOCHEMICAL ANALYSIS OF EOLIAN FLUXES DURING THE TRANSITION FROM GREENHOUSE TO ICEHOUSE CONDITIONS IN EQUATORIAL PACIFIC.

Daniel Nicholas Miller
University of South Carolina - Columbia

GEOCHEMICAL ANALYSIS OF EOLIAN FLUXES DURING THE TRANSITION FROM GREENHOUSE TO ICEHOUSE CONDITIONS IN EQUATORIAL PACIFIC.

by

Daniel Nicholas Miller

Bachelor of Science
University of South Carolina, 2010

Submitted in Partial Fulfillment of the Requirements

For the Degree of Master of Science in

Marine Science

College of Arts and Sciences

University of South Carolina

2014

Accepted by:

Howie Scher, Director of Thesis

Michael Bizimis, Reader

Claudia Benitez-Nelson, Reader

Lacy Ford, Vice Provost and Dean of Graduate Studies

DEDICATION

To my wife, Rebecca, my children, Willow & to be determined…, and my loving pups Casey & Kodiak, may we face and over come many more challenges together.

ACKNOWLEDGEMENTS

I would to thank Howie Scher, my mentor, advisor, and major professor. The opportunity you have given me since my undergraduate career has been unimaginable. You have provided me with many tangibles and intangibles over our time together, lessons and experiences in such a niche field as well as in life. But most of all you instilled a belief and sense of confidence in my work and myself. You allowed me to pursue my curiosity and seek fulfillment of knowledge, even when I couldn't see the woods for the trees. Your gifts will not be spoiled or fleeting,

Next, I would like to thank my committee members Michael Bizimis and Claudia Benitez-Nelson, for making me strive to be a better scientist and researcher. Michael, your presence alone forces me to think, and conduct my research and myself in a more proper manner; thank you for supplying a line when I was stuck in my hole. Claudia, I appreciate you being the constant from when I toured the department as a high school graduate to now, your enthusiasm, support, and success has always been motivating.

Lastly, I would like to thank to my help, predominantly Wayne Buckley, Carl Frisby, Beth Bair, and the Scher lab workers of Patrick Boylan and Zac Moffitt. All of your assistance throughout this process has been greatly appreciated and is irreplaceable.

ABSTRACT

To assess the atmospheric conditions during times of differing pole to equator thermal gradients through the middle Eocene to early Oligocene, 42 to 30 Ma, samples from deep-sea sediment cores U1331, U1332, U1333 from IODP Expedition 320/321 in the eastern equatorial Pacific (EEP) have been chemically leached to isolate the operationally defined eolian dust (ODED; <63 μm fraction). The ODED was analyzed for neodymium (Nd) isotopic compositions and rare earth element (REE) concentrations in order to determine the provenance of the ODED fraction and to elucidate the environmental conditions (e.g. predominant wind patterns) during deposition over the interval of study. The variations in the ODED fraction are expected to be controlled by changes in sources delivered via eolian input. However, negative cerium anomalies in the Post Achaean Australian Shale (PAAS) normalized rare earth element profiles of the ODED show a biasing geochemical seawater phase to the ODED signature. It is found that ε_{Nd} values and cerium anomalies (Ce/Ce*) of ODED are consistent with fossil fish teeth values that record bottom water signatures from the same location and time period until ~36-37 Ma; around the Priabonian/Bartonian boundary marked by increased thermal gradients due to the emplacement of high elevation glaciers on Antarctica (Scher et. al., 2014). Moreover, the more negative cerium anomalies correlate to more radiogenic ε_{Nd}

values. The geochemical seawater signature in the ODED samples is believed to be caused by a change in sedimentary phase regulated by the spatial paleoposition of the sites relative to the biological high productivity zone and/or the depth of the CCD. Subsequently these regulators on the sedimentary phases of the ODED were investigated for biasing the geochemical signatures of the ODED, assumed to be changes in sources thereby provenance. Together, the Nd and REE results from the study temporally indicate that the ODED fraction may be a mixing between two sources, that of a biasing biogenic and/or authigenic source that records seawater conditions, and that of an older, less radiogenic continental source, inferred as Asian loess, as an increased thermal gradient prevails over the course of the study. Further research needs to be performed to make more robust and conclusive linkages between sources, mixing of sources, and atmospheric eolian delivery patterns, highlighting the necessity for a better understanding of atmospheric conditions during important climatic events throughout the history of the Earth.

TABLE OF CONTENTS

LIST OF TABLES

LIST OF FIGURES

LIST OF SYMBOLS

$(^{143}Nd/^{144}Nd)_a$	Sample $^{143}Nd/^{144}Nd$ value normalized to Nd standard JNdi-1 = 0.512115
Ce/Ce*	Cerium Anomaly calculated from PAAS-normalized values as follows: $[Ce/Ce^* = (3Ce_{(n)})/(2La_{(n)} + Nd_{(n)})]$
ε_{Nd}	Epsilon notation of Neodymium relative to CHUR calculated as follows: $10^4*[((^{143}Nd/^{144}Nd)_a/(^{143}Nd/^{144}Nd)_{CHUR})-1]$,
Eu/Eu*	Europrium Anomaly calculated from PAAS-normalized values as follows: $[Eu/Eu^* = (2Eu_{(n)})/(Sm_{(n)} + Gd_{(n)})]$
$La_{(n)}/Yb_{(n)}$	Ratio of LREE to HREE in form of Lanthanum to Ytterbium
Subscript(n)	PAAS-normalized value

LIST OF ABBREVIATIONS

$CaCO_3$ ..... Calcium Carbonate

CAE ..... Carbonate Accumulation Events

CAR ..... Carbonate Accumulation Rates

CCD ..... Calcium Carbonate Compensation Depth

CEMS ..... Center of Elemental Mass Spectrometry

CHUR ..... Chondritic Uniform Reservoir

CO_2 ..... Carbon Dioxide

DSDP ..... Deep Sea Drilling Program

EEP ..... Eastern Equatorial Pacific

EOT ..... Eocene/Oligocene Transition

EPR ..... East Pacific Rise

Fe ..... Iron

HCl ..... Hydrochloric Acid

HF ..... Hydrofluoric Acid

H_2O_2 ..... Peroxide

HNO_3 ..... Nitric Acid

HREE ..... Heavy Rare Earth Elements

ICPMS ..... Inductively Coupled Plasma Mass Spectrometer

IODP ..... Integrated Ocean Drilling Program

ITCZ ..... Intertropical Convergence Zone

La ..... Lanthanum

LREE ..... Light Rare Earth Elements

Ma ..... Mega-annum

MAR ..... Mass Accumulation Rates

MC-ICPMS ..... Multi Collector-Inductively Coupled Plasma Mass Spectrometer

MECO ..... Middle Eocene Climatic Optimum

Mn ..... Manganese

NaOH ..... Sodium Hydroxide

Nd ..... Neodymium

ODED ..... Operationally Defined Eolian Dust

PAAS ..... Post Achaean Australian Shale

PEAT ..... Pacific Equatorial Age Transect

REE ..... Rare Earth Elements

Sm ..... Samarium

SEM ..... Scanning Electron Microscope

XRD ..... X-Ray Diffraction

Yb ..... Ytterbium

CHAPTER 1

INTRODUCTION

The intensity of the global wind systems depends directly upon the pole to equator temperature gradient (Rea & Janecek 1982). Thus the thermal gradient regulates the equatorial trade wind intensities, directly impacting conditions of the equatorial surface ocean (Hovan, 1995). In general, steeper gradients produce stronger winds and more intense upwelling. As the world's largest ocean the equatorial Pacific is a classic example of this linkage, dominated by wind-driven circulation and largely unfettered by continental margins, the strength of the atmospheric and oceanic circulation at the Equator is strongly tied to the global climate system (Palike et. al., 2010). Circulation of the dominant Hadley cell governs latitudinal heat transport between the equatorial zone and 30^{o}N and S, and directly impacts the vigor in which the equatorial surface ocean overturns via Ekman induced upwelling. The large equatorial region of the Pacific supports high productivity due to these winds patterns, delivering nutrients via eolian input and upwelling; resulting in high rates of biological productivity and increased export production (Erhardt et. al., 2013) and enhanced biological drawdown of CO_2 (Pearson et. al., 2009; Coxhall & Wilson, 2011; Erhardt et. al., 2013). The influence of the trade winds on the eastern equatorial Pacific (EEP) is particularly interesting on geological time scales because there is strong evidence that the high productivity zone that is observed today persisted in the past. The equatorial

upwelling zone of the Pacific Ocean is the largest oceanic source of CO_2 to the atmosphere and thereby exerts considerable control on atmospheric CO_2 levels (Dore et al., 2003; Palike et al., 2010). The mound of biogenic sediment (Palike et. al., 2010) that is observable on the seafloor beneath the upwelling zone is testament to the persistence of upwelling on geologically long time scales. Moreover, when sediment cores from the EEP are backtracked to their Paleogene locations the spatial distribution of high mass accumulation rates indicates a zone of high productivity (Moore et. al., 2004).

To explore the temporal linkage between changes in thermal gradients and equatorial atmospheric circulation, the middle Eocene to early Oligocene interval is ideal; representing one of the most significant climate transitions in the Cenozoic, during which greenhouse conditions were supplanted by icehouse conditions of the present day (Jovane et. al., 2009). During this interval of long term cooling there are three main periods of interest: (1) the middle Eocene climatic optimum (MECO), a global short-lived extreme warming event at ca. 40 (Bohaty & Zachos, 2003; Jovane et. al., 2009) thought to be caused by a transient rise in pCO_2 levels (Bohaty & Zachos, 2003) representing a prominent short-lived, peak warming lasting ~500 kyr, essentially a return to early Cenozoic greenhouse climates (Zachos et. al., 2008; Scher & Delaney, 2010); (2) the Priabonian/Bartonian boundary, ~37 Ma, marked by the emplacement of high elevation glaciers on Antarctica (Scher et. al., 2014); (3) the Eocene/Oligocene Transition (EOT), one of the most pronounced climate events during the Cenozoic era, characterized by a period of large-scale continental Antarctic ice

growth, “one cold pole” and a major step from the early Cenozoic greenhouse conditions toward the glaciated climate state of today (Lear et. al, 2008).

Sediment cores drilled during the IODP Expedition 320 were targeted based on their position relative to the equatorial upwelling regime. As the Pacific plate moved to the northwest the drill sites drifted under the upwelling zone, which is often indicated by observable and/or measureable changes in the bulk sediment composition. The sites used in this study, Sites U1331, U1332, and U1333 drifted from -114.36^{o}E, 2.0^{o}N, -113.26^{o}E, 1.94^{o}N, and -110.58^{o}E, 0.75^{o}N around 42 Ma to -120.63^{o}E, 4.27^{o}N, -119.53^{o}E, 4.16^{o}N, and -116.88^{o}E, 2.90^{o}N around 30 Ma, respectively on the Pacific plate (Palike et. al., 2012). Temporally and spatially tethering the sites to the equatorial high productivity zone. In the equatorial Pacific high production is linked to carbonate accumulation events (CAEs) that coincide with increased biogenic silica accumulations rates and shifts between calcareous and siliceous microfossils (Palike et. al., 2012). Consequently due to the increased biogenic growth, changes in the tropic dynamics would follow, seen by a decrease latitudinally from the equator of carbonate fluorapatite and biogenic calcium phosphate during times of high productivity (Toyoda et. al., 1990). The biogenic deposition can be seen in the cores, marked by an increased in calcium carbonate deposition after the EOT. However the preservation of these components is regulated by the calcium carbonate compensation depth (CCD), the depth at which the downward flux of carbonate rain delivered from calcifying organisms is balanced by dissolution, allowing little to no carbonate to be preserved below this depth (Palike et. al.,

2012). During interval of study there are two main features of the CCD, the shoaling during the MECO placing all of the study sites below it, and the deepening during the EOT placing all of the study sites above the depth, with fluctuations in shoalings and CAEs, deepenings, between these two distinct features.

When coupled spatially to the equatorial high productivity zone, preservation or a shift in the calcium carbonate ($CaCO_3$) burial in sediments and therefore relative depth of the CCD can be a function of frequency of high productivity in the region. Regions that experience high production results in a relatively large fraction of $CaCO_3$ surviving to be buried in seafloor sediments, seen by the biogenic mound in the equatorial region. Although regions of both high and low production, will experience increased dissolution, where the region of lower $CaCO_3$ will be depleted of $CaCO_3$ first and thus will have a shallower CCD than that of just the high production region (Lyle et. al., 2005). Hence around the equator in a region of high production the CCD is deeper, and bracketing the equatorial high production region the CCD shoals on either side, making the depth of the CCD spatially dependent on production. Thus, these controls, the positioning relative to the high productivity zone and the depth of the CCD, provide temporal and spatial constraints that may influence the sedimentary phases of the sample sites.

A fraction of the sedimentary phases will be used to provide insight into the equatorial atmospheric circulation, that of eolian dust preserved in deep-sea sediment cores, which is a proven valuable indicator of past atmospheric

circulation and continental paleoclimate (Nakai et. al., 1993; Ziegler et. al., 2007). Eolian dust is transported by wind and is scavenged from the troposphere by precipitation during transportation. Thus, continental dust can be a good tracer of atmospheric circulation and transport based on changes in its spatial deposition patterns, as well as a reliable indicator of climate in the dust's source area (Grousset & Biscaye, 2005; Xie & Marcantonio, 2012). The development of paleoenvironmental reconstructions from the analysis of eolian materials requires the separation of the eolian component from the bulk sediment assemblage (Olivarez et. al., 1991). Therefore the eolian component from the sample sites has been isolated by sequential chemical leaching for geochemical analysis, neodymium (Nd) and rare earth elements (REE) and yttrium. The residual material remaining after the extraction will be referred to as eolian, or as operationally defined eolian dust (ODED) fraction.

Past studies researching eolian input in the Pacific have provided insight resolving possible sources by the use of geochemical isotopic, mineralogical, and grain size analysis. Of particular interest are the previous geochemical studies utilizing isotopic and REE analysis for identifying dust sources and reconstructing atmospheric dispersal pathways (Grousset & Biscaye, 2005; Feng et. al., 2009). The isotopic compositions are significantly different between crustal- and mantle-derived rocks, and these differences are preserved in the detrital windblown fraction of sediments in the deep ocean (Xie & Marcantonio, 2012). These studies have provided the premise and a geochemical record of continental,

volcanogenic, and authigenic sources surrounding the Pacific, that this study looks to build upon.

Therefore there are spatial and temporal constraints that must be accounted for in this study. For this study, variations in the ODED fraction are expected to be controlled by changes in sources delivered via eolian input. However when considering the necessary spatial and temporal constraints, the changes in sedimentary phase in the ODED may also be due to the latitudinal position relative to the high productivity zone and/or the depth of the CCD. Subsequently these controls on the sedimentary phases of the samples are investigated for biasing the geochemical signatures, assumed to be changes in sources thereby provenance. By examination of the latitudinal transect across the equatorial region, the effects of changes in carbonate production, productivity, from changes in bottom water chemistry, dissolution, upon carbonate burial may be separated (Lyle, 2003).

Accordingly, in this study, the aim is twofold: (1) reconstruct broad atmospheric circulation using provenance signals in the ODED component from the middle Eocene to early Oligocene in the EEP during the transition from greenhouse to icehouse conditions, (2) investigate possible biasing regulators on the ODED isotopic signatures and profiles. To do so, the ODED component of deep-sea sediment cores U1331-U1333 drilled during IODP Expedition 320, was isolated and analyzed for Nd and REE concentrations for potential insight regarding provenance of the ODED fraction and the conditions in which it was deposited over the interval of study (Takebe, 2005).

CHAPTER 2

METHODS AND MATERIALS

2.1 SITE DESCRIPTION AND SAMPLING

Samples were recovered during the Integrated Ocean Drilling Program (IODP) Expedition 320, Sites U1331, U1332, and U1333, from a portion of the Pacific Equatorial Age Transect (PEAT), building upon previous drilling (i.e. ODP Legs 138 and 199), see Figure 2.1. The PEAT program was designed to core and recover a continuous Cenozoic record of the equatorial Pacific, providing an age transect of eastern equatorial Pacific sediments deposited within $\pm 2^{o}$ of the Equator on the Pacific plate, documenting the Pacific equatorial biogenic mound (Palike et. al., 2010). The study sites are not influenced by hemipelagic sedimentation, turbidity sedimentation, and ice rafting, following the sampling strategy of Rea et. al., (1985) & Olivarez et. al., (1991).

The MECO in the study Sites U1331-U1333 is marked by a shoaling of the CCD, which is illustrated in the lithostratigraphy by showed by alternating sequences of nannofossil ooze, radiolarian nannofossil ooze, and nannofossil radiolarian ooze broken by an interval of radiolarian clay. All of the sites illustrate a transition from darker brown sediments of the Eocene to the white to pale brown nannofossil ooze of the earliest Oligocene age, evidence of the drop in the CCD associated with the EOT. This can further be seen, Figure 2.2, by the

increase in the carbonate accumulation rates (CAR) and $CaCO_3$ weight percent (Palike et. al., 2010). The lithostratigraphy of the cores during the EOT is as follows, U1331 abruptly transitioned from carbonates to dark brown clayey radiolarian ooze, while U1332 and U1333 transitioned through radiolarian nannofossil ooze to radiolarian ooze with clay or clayey radiolarian ooze. Note that in Site U1333 at the EOT boundary, there was presence of volcanic shards (>75 μm) (Kuroda, 2013). (Palike et. al., 2010) The sampling resolution for Sites U1331, U1332, and U1333 were 250 ka, 240 ka, and 240 ka (180 ka with high resolution sampling from U1333B spanning 36-37 Ma, averaging 40 ka) respectively.

2.2 Physical Sample Separation

Separation via grain size classification of grains less than 63 μm is believed to best represent the eolian fraction (Eisenhauer et. al., 1999). Therefore the bulk core samples were dried to evaporate any existing water contained in the sample, allowing for easier disaggregation during the sieving process. The samples were sorted by grain size by washing with distilled water through a 125-μm and 63 μm sieve, utilizing an automatic sample washer designed by Jason Curtis at the University of Florida. The less than 63-μm size fraction, was collected, covered, and set aside, allowing the sediment to settle. Once settled, overlying waters were siphoned off without perturbation of the sediment. The remaining overlying waters were agitated; sediment was re-

suspended, and transferred to a centrifuge tube. The samples were centrifuged and then dried down.

2.3 Sequential Extraction

Sequential chemical extraction based on Bayon et al. (2002) to define the ODED was performed on all samples. Approximately 0.2 grams of bulk sample were weighed out and placed in centrifuge tubes. Samples were decarbonated by use of 25% buffered acetic acid (50 mls per gram). Samples were then centrifuged, decanted, and triple rinsed with milliQ water. The ferromanganese coatings were leached by 1 M hydroxylamine hydrochloride in 25% acetic acid (35 mls per gram). Samples were then centrifuged, decanted and triple rinsed with milliQ water. Lastly samples were immersed in 5% peroxide (H_2O_2) overnight to remove any organic carbon. Samples were centrifuged, decanted and triple rinsed with milliQ water, then dried.

Roughly 20 samples from Site U1332 spanning in age from ~33-39 Ma were selected for analysis utilizing a different sequential chemical leach used to isolate the terrigenous and ODED fraction of deep-sea sediment cores based on studies like Rea & Janecek (1981), Hovan & Rea (1992), and Olivarez and Lyle (2002). First samples were treated with 25% acetic acid and placed on a mechanical rocker for 2 hours to remove carbonates. Samples were then centrifuged, decanted, and treated with 25% acetic acid for a second time. Samples were centrifuged, decanted and rinsed with ~80^{o}C milliQ water twice. Next opal was removed by immersing samples in 1.5 M sodium hydroxide

(NaOH) and in a ~85^{o} hot bath for 2 hours, stirring solutions every hour. Samples were then centrifuged and decanted. The oxide/hydroxide extraction followed, where 0.3 M sodium citrate was added to each tube with 1 M sodium bicarbonate and placed in a hot water bath for 15 minutes. Sodium dithionite was then added to each sample, stirred, and returned to the hot water bath. After 10 minutes, a 50/50 solution of milliQ water and 0.3 M sodium citrate, was added, stirred, centrifuged and decanted. The oxide/hydroxide extraction was preformed twice. The samples next underwent a ~80^{o}C 0.3 M sodium citrate rinse twice, followed by three hot milliQ water rinses. Lastly, samples were treated with four more, ~80^{o}C milliQ water rinses.

2.4 Sample Digestion and Gravitational Chromatography

The leached samples were split into two aliquots, one for isotopic analysis and the other for elemental analysis. All aliquots were chemically digested in the clean lab in the Center of Elemental Mass Spectrometry (CEMS lab) at the University of South Carolina.

First ~7 mg of leached samples were weighed in Teflon vials. Then 1 ml of nitric acid (HNO_3) and hydrofluoric acid (HF) mixture, 1:3 parts respectively, was added to each sample. The samples were then capped and placed on heat in a flow box for 2-3 days. Upon visual inspection of samples for complete digestion, the samples were uncapped and dried down. Once dried, 0.5 ml of concentrated HNO_3 was added to each sample to eliminate any trace HF, and placed in the flow down boxes on heat until dried.

The aliquots for isotope analysis were reconstituted in 250 μl of 2.5 M HCl and ran through BioRad cation exchange columns, filled with 2 ml of AG50W-X2, analytical grade cation exchange resin with a mesh size of 200-400 μm, to isolate the REE from major cations. Nd was then purified from the REE by the procedure of Scher and Delaney (2010) utilizing Ln-Spec resin (100-150 μm).

The aliquots for elemental analysis were reconstituted in 2% HNO_3 following digestion and dilution factors (~1:50,000) calculated for analysis on the Thermo Finnigian Element 2 ICP/MS.

2.5 Analytical Methods

A multi collector inductively coupled plasma mass spectrometer Thermo Neptune (MC-ICPMS), at the CEMS laboratory at the University of South Carolina preformed the Nd isotopic analyses. Samples were measured with high sensitivity using an APEX inlet system. During analysis, isobaric interferences, ^{147}Sm & ^{149}Sm, for Nd were monitored. To ensure accuracy, all Nd values are normalized to Nd standard JNDi-1, 0.512115. Nd standard JNdi-1 during the period of the study had a mean value of $^{143}Nd/^{144}Nd = 0.512113 \pm 0.00002$ (2σ, n=113).

REE analyses of ODED fraction were performed on the Thermo Finnigian Element 2 ICP/MS, also at the CEMS laboratory for suite of elements and REEs. Measurements were made in high resolution to decrease and account for possible oxides. Normalized values are relative to Post Achaean Australian Shale (Taylor & McClennan, 1985).

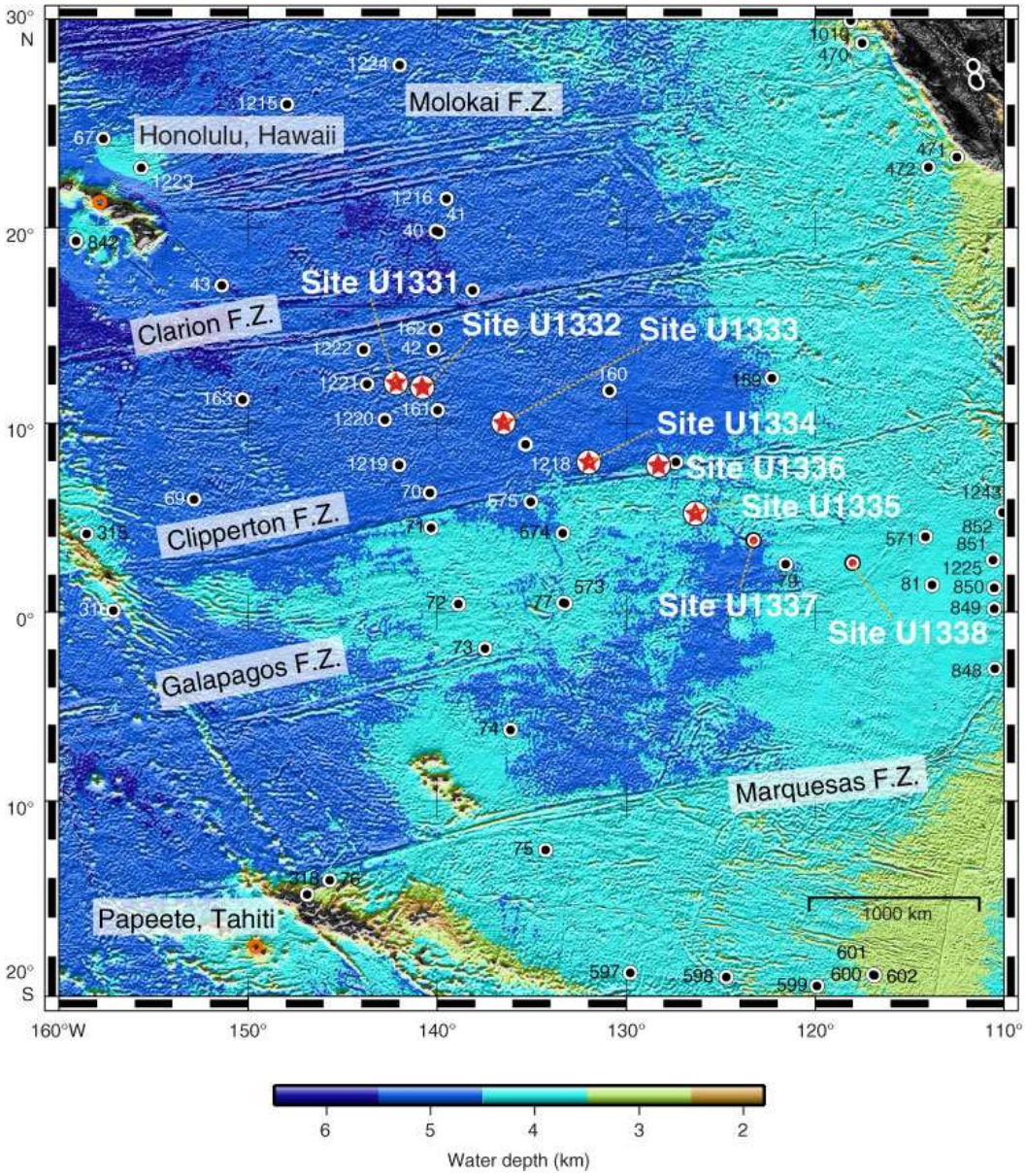

Figure 2.1. Present day IODP Expedition 320/321 Site locations on a present day bathymetric map in the Eastern Equatorial Pacific (Palike et. al., 2010).

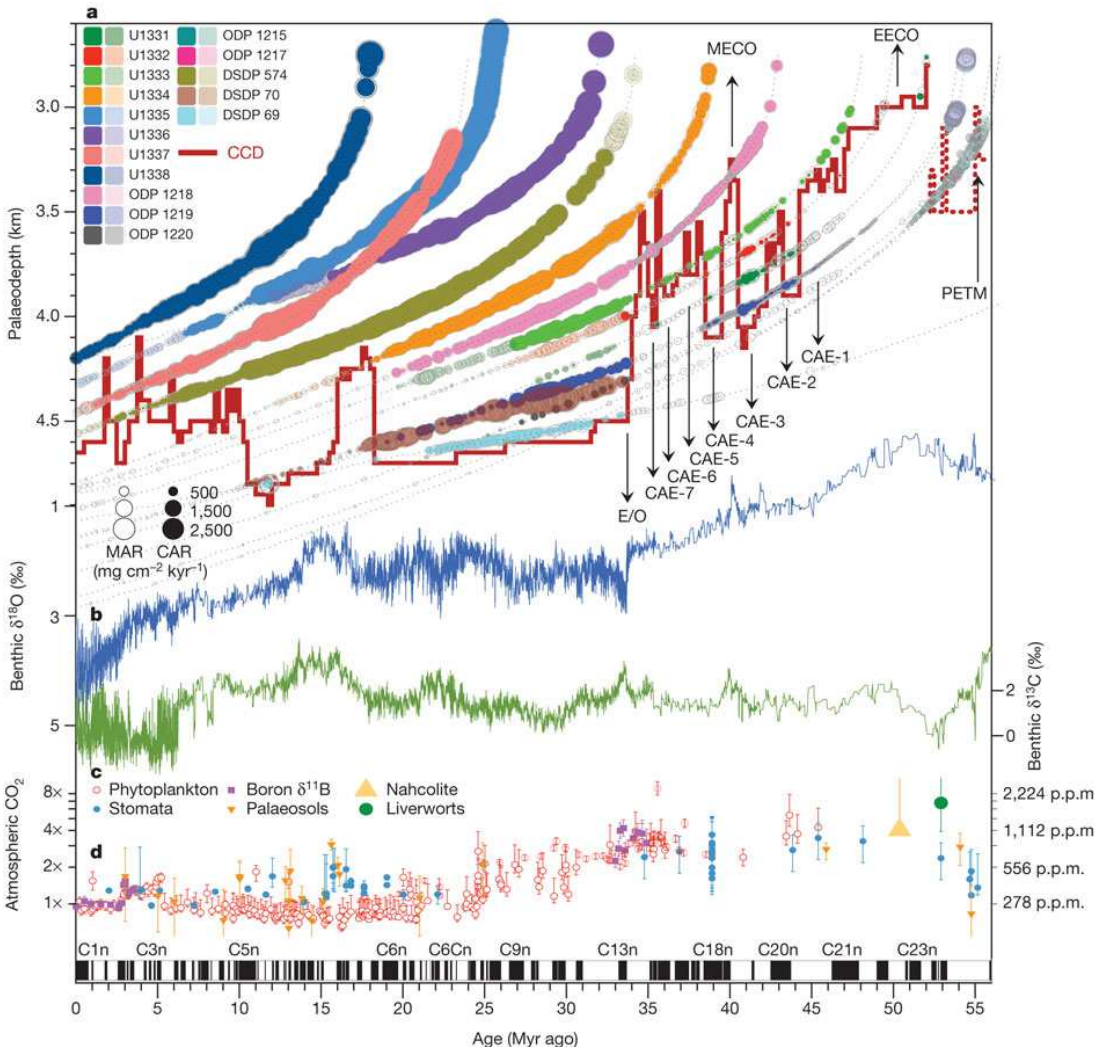

Figure 2.2. Paleodepths, Mass Accumulation Rates (MAR), and Carbonate Accumulation Rates (CAR) of IODP Expedition 320/321 Site locations, relative to the measured Carbonate Compensation Depth (CCD) relative to $\delta^{18}O$ and CO_2 concentrations over time (Palike et. al., 2012).

CHAPTER 3

RESULTS

3.1 ND ISOTOPES

Overall the ε_{Nd} values of the ODED samples from all study sites become less radiogenic over the study interval (Figure 3.1). During the MECO, Sites U1331 & U1332 ε_{Nd} values peak from ~-4.25 to a more radiogenic -3, then trend to less radiogenic values. Site U1333 during the MECO ranges from -4.25 to -4.5, absent of a prominent more radiogenic peak like that of Sites U1331 & U1332. At ~37-36 Ma, ε_{Nd} values for all sites are in agreement, becoming less radiogenic, decreasing from -4.75 to -5.25. After ~36 Ma, Site U1331 steadily decreases from -5.25 to -6 around 43.5 Ma, remaining at -6 until 31.5 Ma where it then spikes to a less radiogenic value of -6.6, gradually returning to -6 over the remaining 2 Ma of the interval of study. As for Site U1332 and U1333 after the tail end of the agreement at ~36 Ma, the variability of the ε_{Nd} values increases, unlike that of Site U1331. Site U1332 is the most variable after 36 Ma and most radiogenic, ranging in ε_{Nd} values, -6 to -3.4, from 36 Ma to 32.5 Ma. After which Site U1332 values range from -5.25 to -7. Similarly Site U1333 ε_{Nd} values range from -5.5 to -8, fluctuating from -5.5 to less radiogenic values. For most samples after 34 Ma, Site U1333 has the least radiogenic values of all sites.

3.2 REE PROFILES

ODED samples from all sites and terrigenous extraction residues from Site U1332 have prominent negative cerium anomalies indicative of seawater. Figure 3.2c shows the abundance of the negative cerium anomalies in the samples, mainly spanning 42 Ma to ~36 Ma, seen in red and orange, supported by Figure 3.3a. The ODED's negative cerium anomalies decrease over time, ranging from 0.2 (42 Ma) to 0.8 (30 Ma), showing that during the period of study the ODED samples are never absent of a negative cerium anomaly. The terrigenous extracted residues' negative cerium anomalies range from 0.4 (38 Ma) to, little or no negative anomaly to a positive anomaly, 0.8-1 or greater (37–32 Ma). From 34 to 30 Ma the greatest abundance of least negative cerium anomalies, greater than 0.6, occurs for all sites, represented in blue in Figure 3.2b.

The most negative cerium anomalies, 0.2-0.4, correlate with high $La_{(n)}/Yb_{(n)}$ ratios, spanning 42-38 Ma, Figure 3.3a & 3.3b. The $La_{(n)}/Yb_{(n)}$ ratios presented for all ODED samples decrease from greater than 1 to ~0.5 over the course ~4 Ma from 42 Ma to 38 Ma, showing a decrease in the enrichment of LREE relative to the HREE. Subsequently samples from all sites for both extractions, gradually increase after 38 Ma, from ~0.5 to 0.8, increasing in the enrichment of LREE relative to HREE. There is mainly agreement between all sites and the different extractions in regards to $La_{(n)}/Yb_{(n)}$ ratios and europium anomalies.

A positive europium anomaly is seen in all ODED samples, Figure 3.3c, and in terrigenous extraction residues. The europium anomaly peaks from ~1.25

to 2 over the period of 42-39 Ma for all sites. After 39 Ma till ~33 Ma, the europium anomaly ranges from 1.25 to ~1.5. At ~33 Ma, Site U1333 differs from the other two sites, with an europium anomaly increasing from 1.5 to 2.5 at 32 Ma, to quickly decrease back to 1.25.

3.3 Comparison of ODED & Terrigenous Extraction Residues

Figure 3.4 shows the relationship between the two different leaches with respect to Nd. Roughly half of the samples are within 2 standard error of the 2σ error envelope, 6 of which that plot along the 1:1 line, Figure 3.4b. Besides the samples that fall on the 1:1 line, the ODED extraction provides $^{143}Nd/^{144}Nd$ values, thus ε_{Nd} values that are more radiogenic than that of the less radiogenic terrigenous extraction. The ODED ε_{Nd} values, peaking from -5.5 to -4 to return, differ most from the terrigenous residues, ε_{Nd} values of -6, from 37 Ma to ~34 Ma, Figure 3.4a. Moreover the ODED samples are associated with greater negative cerium anomalies, ranging from 0.3-0.7 than that of the same samples extracted by the terrigenous method, 0.4-1.2, Figure 3.4c. This plot summarizes the difference between residues operationally extracted, with respect to the ε_{Nd} and the corresponding cerium anomalies; where the terrigenous extraction provides residues that range from -4 to -8 with less of a cerium anomaly, 0.4-1.2, whereas the ODED extraction is more radiogenic, -3.5 to -6, with more negative cerium anomalies ranging from 0.3-0.7; closer to that of seawater values derived from fossil fish teeth from the same period of time, the grayed region. This is further seen in Figure 3.5, where all of the ODED samples are represented on the same

graph in relation to the terrigenous extraction, showing that all of the ODED samples have a relationship with the cerium anomaly, being that the more radiogenic ε_{Nd} values correlate with the more negative cerium anomalies. This trend does not hold true for the terrigenous extracted samples, that fall close and along the line of no cerium anomaly, showing samples have little to no negative anomaly associated with it.

3.4 Relationship of ODED ε_{ND} values & Cerium Anomalies

As mentioned above, Figure 3.5 shows that more radiogenic ε_{Nd} values are associated with greater negative cerium anomalies. Additionally from Figure 3.6, ε_{Nd} values and cerium anomalies show a correlation relative to time. Progressing from 42 Ma to 30 Ma, the ε_{Nd} values for all sites become increasingly less radiogenic, from ε_{Nd} values of -3 to -8, as the cerium anomalies become increasingly less negative, progressing from 0.2 to 0.8.

Table 3.1. Neodymium Isotope Results of Site U1331 ODED Samples

	Core, section, interval	Depth (CSF)	Depth (CCSF)	Age (Ma) [GTS 2012]	143Nd/144Nda	2SEM	εNd(0)	2SEM
Hole U1331A-								
	2H-5, 75-76	11.95	13.45	29.42	0.512328	0.000003	-6.05	0.06
	2H-6, 75-76	13.45	14.95	29.97	0.512297	0.000004	-6.65	0.07
	2H-7, 25-26	14.45	15.95	30.43	0.512311	0.000002	-6.38	0.04
	3H-1, 100-101	15.7	18.61	31.32	0.512341	0.000003	-5.78	0.05
	3H-2, 100-101	17.2	20.11	31.63	0.512295	0.000003	-6.69	0.06
	3H-3, 100-101	18.7	21.61	31.94	0.512322	0.000004	-6.16	0.07
	3H-4, 100-101	20.2	23.11	32.25	0.512326	0.000003	-6.09	0.06
	3H-5, 100-101	21.7	24.61	32.56	0.512329	0.000002	-6.03	0.05
	3H-6, 100-101	23.2	26.11	32.87	0.512322	0.000003	-6.16	0.06
	4H-2, 75-76	26.45	29.71	33.90	0.512345	0.000003	-5.71	0.06
	4H-3, 75-76	27.95	31.21	34.36	0.512330	0.000003	-6.01	0.05
	4H-4, 75-76	29.45	32.71	34.82	0.512344	0.000003	-5.73	0.05
	4H-5, 75-76	30.95	34.21	35.33	0.512339	0.000003	-5.83	0.06
	4H-7, 65-66	33.85	37.11	35.95	0.512368	0.000005	-5.27	0.10
	5H-1, 75-76	34.45	39.7	36.07	0.512343	0.000004	-5.75	0.08
	5H-2, 75-76	35.95	41.2	36.34	0.512366	0.000004	-5.31	0.07
	5H-3, 75-76	37.45	42.7	36.61	0.512363	0.000004	-5.36	0.09
	5H-4, 75-76	38.95	44.2	36.87	0.512377	0.000005	-5.09	0.10
	5H-5, 75-76	40.45	45.7	37.10	0.512399	0.000004	-4.65	0.09
	5H-6, 75-76	41.95	47.2	37.32	0.512407	0.000005	-4.51	0.10
	5H-7, 8-9	42.28	47.53	37.37	0.512396	0.000005	-4.72	0.09
	6H-1, 75-76	43.95	51.11	37.96	0.512402	0.000004	-4.60	0.07
	6H-2, 75-76	45.45	52.61	38.24	0.512376	0.000003	-5.11	0.06
	6H-3, 75-76	46.95	54.11	38.51	0.512371	0.000004	-5.21	0.08
	6H-4, 75-76	48.45	55.61	38.70	0.512417	0.000004	-4.31	0.08
	6H-5, 75-76	49.95	57.11	38.83	0.512406	0.000017	-4.52	0.34
	6H-6, 60-61	51.3	58.46	38.95	0.512423	0.000008	-4.20	0.16
	6H-7, 30-31	52	59.16	39.02	0.512403	0.000011	-4.59	0.21
	7H-2, 75-76	54.95	64.76	39.52	0.512472	0.000006	-3.24	0.12
	7H-3, 75-76	56.45	66.26	39.65	0.512466	0.000006	-3.36	0.12
	7H-4, 75-76	57.95	67.76	39.75	0.512429	0.000006	-4.07	0.12
	7H-5, 75-76	59.45	69.26	39.86	0.512466	0.000004	-3.35	0.07
	7H-6, 75-76	60.95	70.76	39.96	0.512491	0.000007	-2.86	0.14
	7H-7, 30-31	62	71.81	40.04	0.512405	0.000006	-4.55	0.11
	Duplicate				0.512407	0.000008	-4.50	0.15
	8H-1, 75-76	62.95	73.72	40.16	0.512417	0.000005	-4.32	0.10
	Duplicate				0.512442	0.000005	-3.82	0.09
	8H-2, 75-76	64.45	75.22	40.23	0.512456	0.000008	-3.55	0.16
	Duplicate				0.512460	0.000004	-3.47	0.08
	8H-3, 75-76	65.95	76.72	40.30	0.512404	0.000004	-4.57	0.08
	8H-4, 75-76	67.45	78.22	40.37	0.512418	0.000013	-4.29	0.25
	Duplicate				0.512444	0.000007	-3.79	0.13
	8H-5, 75-76	68.95	79.72	40.44	0.512421	0.000004	-4.23	0.08
	Duplicate				0.512470	0.000009	-3.28	0.18
	8H-6, 75-76	70.45	81.22	40.52	0.512410	0.000006	-4.44	0.11
	Duplicate				0.512417	0.000012	-4.32	0.24
	8H-7, 40-41	71.6	82.37	40.57	0.512423	0.000005	-4.19	0.10
	Duplicate				0.512414	0.000005	-4.37	0.10
	9H-4, 74-75	76.94	88.3	40.85	0.512420	0.000007	-4.26	0.13
	9H-5, 75-76	78.45	89.81	40.92	0.512418	0.000004	-4.28	0.09
	9H-6, 75-76	79.95	91.31	40.99	0.512405	0.000006	-4.54	0.12
	9H-7, 55-56	81.25	92.61	41.05	0.512364	0.000018	-5.34	0.36
a. All data are normalized to Jndi-1 = 0.512115								

Table 3.2. Neodymium Isotope Results of Site U1332 ODED Samples

	Core, section, interval	Depth (CSF)	Depth (CCSF)	Age (Ma) [GTS 2012]	143Nd/144Nda	2SEM	εNd(0)	2SEM
Hole U1332A-								
	6H-3, 75-76	45.65	51.15	29.44	0.512325	0.000005	-6.10	0.09
	6H-4, 75-76	47.15	52.65	29.73	0.512325	0.000005	-6.11	0.09
	6H-5, 75-76	48.65	54.15	30.04	0.512275	0.000004	-7.07	0.09
	6H-6, 75-76	50.15	55.65	30.33	0.512326	0.000004	-6.08	0.08
	6H-7, 35-36	51.25	56.75	30.54	0.512337	0.000003	-5.88	0.06
	7H-1, 75-76	52.15	59.9	31.15	0.512368	0.000004	-5.26	0.08
	7H-2, 75-76	53.65	61.4	31.35	0.512333	0.000005	-5.95	0.10
	7H-3, 75-76	55.15	62.9	31.55	0.512370	0.000006	-5.23	0.11
	7H-4, 75-76	56.65	64.4	31.75	0.512278	0.000004	-7.02	0.07
	7H-5, 75-76	58.15	65.9	31.95	0.512273	0.000004	-7.12	0.09
	7H-6, 75-76	59.65	67.4	32.15	0.512355	0.000004	-5.52	0.08
	7H-7, 35-36	60.75	68.5	32.29	0.512273	0.000005	-7.12	0.09
	8H-2, 75-76	63.15	70.5	32.56	0.512386	0.000008	-4.92	0.15
	8H-3, 75-76	64.65	72	32.76	0.512326	0.000005	-6.08	0.09
	8H-4, 75-76	66.15	73.5	32.96	0.512367	0.000006	-5.29	0.11
	8H-5, 75-76	67.65	75	33.16	0.512328	0.000004	-6.05	0.07
	8H-6, 75-76	69.15	76.5	33.43	0.512341	0.000004	-5.79	0.08
	8H-7, 35-36	70.25	77.6	33.64	0.512338	0.000009	-5.86	0.18
	9H-1, 75-76	71.15	73.78	33.00	0.512468	0.000003	-3.32	0.06
	9H-2, 75-76	72.65	75.28	33.21	0.512348	0.000004	-5.66	0.09
	9H-3, 75-76	74.15	76.78	33.48	0.512410	0.000006	-4.45	0.11
	9H-4, 75-76	75.65	78.28	33.80	0.512389	0.000003	-4.86	0.06
	9H-5, 75-76	77.15	79.78	34.26	0.512348	0.000005	-5.65	0.10
	9H-6, 75-76	78.65	81.28	34.73	0.512396	0.000004	-4.71	0.09
	9H-7, 35-36	79.75	82.38	35.06	0.512436	0.000006	-3.94	0.12
	10H-1, 85-86	80.75	84.05	35.51	0.512417	0.000004	-4.32	0.08
	10H-2, 75-76	82.15	85.45	35.86	0.512380	0.000004	-5.04	0.09
	10H-3, 75-76	83.65	86.95	36.22	0.512356	0.000003	-5.51	0.06
	10H-4, 75-76	85.15	88.45	36.54	0.512383	0.000005	-4.97	0.10
	10H-5, 75-76	86.65	89.95	36.83	0.512383	0.000005	-4.97	0.09
	10H-6, 75-76	88.15	91.45	37.08	0.512392	0.000005	-4.80	0.09
	10H-7, 40-41	89.3	92.6	37.26	0.512442	0.000007	-3.82	0.14
	11H-2, 75-76	91.65	95.03	37.63	0.512403	0.000003	-4.58	0.07
	11H-3, 75-76	93.15	96.53	37.92	0.512450	0.000006	-3.66	0.12
	Duplicate				0.512423	0.000007	-4.20	0.13
	11H-4, 75-76	94.65	98.03	38.21	0.512438	0.000006	-3.91	0.12
	11H-5, 75-76	96.15	99.53	38.53	0.512437	0.000005	-3.92	0.09
	12H-2, 75-76	101.15	107.37	39.53	0.512427	0.000004	-4.12	0.08
	12H-3, 75-76	102.65	108.87	39.70	0.512428	0.000007	-4.09	0.13
	12H-4, 75-76	104.15	110.37	39.88	0.512425	0.000009	-4.15	0.18
	12H-5, 75-76	105.65	111.87	40.06	0.512399	0.000007	-4.67	0.14
	12H-6, 65-66	107.05	113.27	40.20	0.512482	0.000010	-3.04	0.19
	12H-7, 35-36	108.05	114.27	40.27	0.512421	0.000008	-4.24	0.17
	13H-1, 75-76	109.15	117.77	40.54	0.512421	0.000006	-4.23	0.12
	13H-2, 75-76	110.65	119.27	40.65	0.512426	0.000009	-4.13	0.17
	13H-3, 75-76	112.15	120.77	40.77	0.512416	0.000005	-4.32	0.10
	13H-4, 75-76	113.65	122.27	40.88	0.512430	0.000006	-4.06	0.13
	13H-5, 75-76	115.15	123.77	41.00	0.512426	0.000005	-4.13	0.10
	13H-7, 65-66	118.05	126.67	41.23	0.512436	0.000008	-3.94	0.15
	14H-2, 75-76	120.15	132.65	41.79	0.512421	0.000006	-4.23	0.12
	14H-4, 75-76	123.15	135.65	42.06	0.512391	0.000005	-4.82	0.09
	14H-5, 75-76	124.65	137.15	42.20	0.512395	0.000006	-4.74	0.11
	14H-6, 30-31	125.7	138.2	42.30	0.512382	0.000006	-4.99	0.12
a. All data are normalized to Jndi-1 = 0.512115								

Table 3.3. Neodymium Isotope Results of Site U1333 ODED Samples

	Core, section, interval	Depth (CSF)	Depth (CCSF)	Age (Ma) [GTS 2012]	143Nd/144Nda	2SEM	εNd(0)	2SEM
Hole U1333A-								
	8H-7, 45-46	75.75	89.13	29.88	0.512311	0.000007	-6.39	0.14
	9H-1, 75-76	76.75	92.48	30.16	0.512255	0.000005	-7.46	0.10
	9H-2, 75-76	78.25	93.98	30.28	0.512284	0.000005	-6.91	0.10
	9H-3, 75-76	79.75	95.48	30.41	0.512277	0.000004	-7.05	0.08
	9H-4, 75-76	81.25	96.98	30.53	0.512298	0.000005	-6.62	0.10
	9H-5, 75-76	82.75	98.48	30.66	0.512326	0.000007	-6.08	0.13
	9H-6, 75-76	84.25	99.98	30.80	0.512358	0.000007	-5.46	0.14
	9H-7, 55-56	85.55	101.28	30.92	0.512275	0.000005	-7.09	0.09
	10H-1, 75-76	86.25	103.61	31.13	0.512235	0.000005	-7.87	0.10
	10H-2, 75-76	87.75	105.11	31.25	0.512286	0.000007	-6.88	0.14
	10H-3, 75-76	89.25	106.61	31.38	0.512298	0.000006	-6.64	0.12
	10H-4, 75-76	90.75	108.11	31.50	0.512251	0.000005	-7.55	0.11
	10H-5, 75-76	92.25	109.61	31.63	0.512272	0.000004	-7.13	0.09
	10H-6, 75-76	93.75	111.11	31.75	0.512273	0.000007	-7.12	0.14
	10H-7, 40-41	94.9	112.26	31.85	0.512299	0.000007	-6.62	0.14
	11X-1, 75-76	95.75	114.47	32.03	0.512299	0.000006	-6.61	0.12
	11X-2, 75-76	97.25	115.97	32.16	0.512321	0.000006	-6.19	0.12
	11X-3, 75-76	98.75	117.47	32.29	0.512322	0.000009	-6.16	0.17
	11X-4, 75-76	100.25	118.97	32.41	0.512324	0.000008	-6.13	0.15
	12X-1, 105-106	101.75	121.2	32.60	0.512285	0.000006	-6.88	0.12
	12X-2, 75-76	102.95	122.4	32.70	0.512297	0.000007	-6.65	0.14
	12X-3, 75-76	104.45	123.9	32.82	0.512360	0.000021	-5.43	0.40
	12X-4, 75-76	105.95	125.4	32.95	0.512303	0.000004	-6.53	0.08
	12X-5, 75-76	107.45	126.9	33.08	0.512361	0.000009	-5.40	0.17
	13X-1, 70-71	111	132.35	33.65	0.512326	0.000006	-6.08	0.11
	13X-2, 60-61	112.4	133.75	34.02	0.512308	0.000005	-6.43	0.09
	13X-3, 75-76	114.05	135.4	34.58	0.512368	0.000004	-5.27	0.08
	13X-4, 75-76	115.55	136.9	35.18	0.512358	0.000012	-5.46	0.23
	14X-1, 75-76	120.75	142.36	36.53	0.512372	0.000005	-5.18	0.11
	14X-2, 75-76	122.25	143.86	36.75	0.512372	0.000005	-5.19	0.09
	14X-3, 75-76	123.75	145.36	36.99	0.512390	0.000024	-4.84	0.46
	14X-4, 75-76	125.25	146.86	37.26	0.512384	0.000007	-4.95	0.15
	14X-5, 75-76	126.75	148.36	37.52	0.512412	0.000018	-4.40	0.35
	14X-7, 30-31	129.3	150.91	37.94	0.512386	0.000013	-4.92	0.26
	15X-1, 75-76	130.35	155.05	38.59	0.512391	0.000007	-4.83	0.13
	15X-2, 75-76	131.85	156.55	38.76	0.512383	0.000004	-4.98	0.08
	15X-3, 75-76	133.35	158.05	38.94	0.512372	0.000011	-5.18	0.21
	15X-4, 75-76	134.85	159.55	39.11	0.512362	0.000007	-5.38	0.14
	15X-5, 75-76	136.35	161.05	39.28	0.512368	0.000007	-5.27	0.14
	15X-6, 75-76	137.85	162.55	39.45	0.512381	0.000008	-5.01	0.15
	16X-1, 75-76	139.95	165.95	39.90	0.512391	0.000005	-4.81	0.10
	16X-2, 75-76	141.45	167.45	40.13	0.512400	0.000006	-4.65	0.11
	16X-3, 75-76	142.95	168.95	40.26	0.512412	0.000006	-4.40	0.11
	16X-4, 75-76	144.45	170.45	40.39	0.512406	0.000012	-4.53	0.23
	16X-5, 75-76	145.95	171.95	40.52	0.512411	0.000004	-4.42	0.08
	16X-6, 75-76	147.45	173.45	40.64	0.512400	0.000007	-4.64	0.13
	16X-7, 30-31	148.5	174.5	40.73	0.512433	0.000005	-4.00	0.11
	17X-1, 75-76	149.55	177.75	41.01	0.512420	0.000004	-4.25	0.08
	17X-2, 75-76	151.05	179.25	41.13	0.512437	0.000007	-3.92	0.14
	17X-3, 75-76	152.55	180.75	41.32	0.512425	0.000007	-4.16	0.13
	17X-4, 75-76	154.05	182.25	41.61	0.512410	0.000004	-4.44	0.08
	17X-5, 75-76	155.55	183.75	41.93	0.512412	0.000005	-4.41	0.09
	17X-6, 75-76	157.05	185.25	42.26	0.512425	0.000009	-4.16	0.18
Hole U1333B-								
	14H-1, 62-64	122.32	141.77	36.45	0.512371	0.000003	-5.21	0.07
	14H-1, 112-114	122.82	142.27	36.52	0.512367	0.000003	-5.29	0.07
	14H-1, 137-139	123.07	142.52	36.56	0.512377	0.000003	-5.09	0.06
	14H-2, 12-14	123.32	142.77	36.59	0.512369	0.000004	-5.26	0.07
	14H-2, 37-39	123.57	143.02	36.63	0.512382	0.000005	-5.00	0.10
	14H-2, 62-64	123.82	143.27	36.66	0.512367	0.000004	-5.29	0.07
	14H-2, 87-89	124.07	143.52	36.70	0.512381	0.000004	-5.02	0.08
	14H-2, 103-105	124.23	143.68	36.73	0.512398	0.000005	-4.68	0.11
	14H-2, 112-114	124.32	143.77	36.74	0.512406	0.000004	-4.53	0.08
	14H-2, 137-139	124.57	144.02	36.78	0.512372	0.000005	-5.18	0.09
	14H-3, 12-14	124.82	144.27	36.82	0.512376	0.000004	-5.11	0.07
	14H-3, 37-39	125.07	144.52	36.86	0.512393	0.000004	-4.77	0.08
	14H-3, 63-65	125.33	144.78	36.90	0.512387	0.000004	-4.90	0.08
	14H-3, 87-89	125.57	145.02	36.94	0.512375	0.000004	-5.14	0.07
	14H-3, 112-114	125.82	145.27	36.98	0.512386	0.000005	-4.92	0.10
	14H-3, 139-141	126.09	145.54	37.03	0.512389	0.000005	-4.86	0.09
a. All data are normalized to Jndi-1 = 0.512115								

Table 3.4. Neodymium Isotope Results of Terrigenous Extraction Residues

	Core, section, interval	Depth (CSF)	Depth (CCSF)	Age (Ma) [GTS 2012]	143Nd/144Nda	2SEM	εNd(0)	2SEM
Terrigenous Ext. from Hole U1332A								
	8H-4, 75-76	66.15	73.50	32.96	0.512379	0.000008	-5.06	0.16
	8H-5, 75-76	67.65	75.00	33.16	0.512271	0.000011	-7.15	0.22
	8H-6, 75-76	69.15	76.50	33.43	0.512349	0.000011	-5.63	0.22
	9H-1, 75-76	71.15	73.78	33.00	0.512438	0.000006	-3.89	0.12
	9H-2, 75-76	72.65	75.28	33.21	0.512342	0.000017	-5.77	0.33
	9H-4, 75-76	75.65	78.28	33.80	0.512312	0.000010	-6.37	0.19
	9H-5, 75-76	77.15	79.78	34.26	0.512340	0.000015	-5.81	0.29
	9H-6, 75-76	78.65	81.28	34.73	0.512243	0.000004	-7.70	0.08
	9H-7, 35-36	79.75	82.38	35.06	0.512324	0.000004	-6.12	0.08
	10H-1, 85-86	80.75	84.05	35.51	0.512316	0.000016	-6.29	0.31
	10H-2, 75-76	82.15	85.45	35.86	0.512320	0.000012	-6.20	0.23
	10H-3, 75-76	83.65	86.95	36.22	0.512317	0.000010	-6.26	0.20
	10H-4, 75-76	85.15	88.45	36.54	0.512346	0.000018	-5.69	0.36
	10H-5, 75-76	86.65	89.95	36.83	0.512379	0.000013	-5.05	0.24
	10H-6, 75-76	88.15	91.45	37.08	0.512400	0.000018	-4.65	0.35
	10H-7, 40-41	89.30	92.60	37.26	0.512393	0.000007	-4.78	0.13
	11H-2, 75-76	91.65	95.03	37.63	0.512378	0.000006	-5.07	0.12
	11H-3, 75-76	93.15	96.53	37.92	0.512395	0.000008	-4.74	0.15
	11H-4, 75-76	94.65	98.03	38.21	0.512392	0.000015	-4.81	0.29
	11H-5, 75-76	96.15	99.53	38.53	0.512386	0.000016	-4.91	0.31
	11H-6, 75-76	97.65	101.03	38.75	0.512383	0.000007	-4.97	0.13
a. All data are normalized to Jndi-1 = 0.512115								

Table 3.5. Rare Earth Element Concentration Results of Site U1331 ODED Samples

	Core, section, interval	Depth (CSF)	Depth (CCSF)	Age (Ma) [GTS 2012]	La	Ce	Pr	Nd	Sm	Eu	Gd	Tb	Dy	Y	Ho	Er	Tm	Yb	Lu
Hole U1331A-																			
	2H-5, 75-76	11.95	13.45	29.42	16.25	27.67	3.23	13.60	2.54	0.60	2.08	0.41	2.40	18.07	0.54	1.83	0.27	1.70	0.26
	2H-7, 25-26	14.45	15.95	30.43	22.02	30.55	4.36	19.84	4.03	0.94	3.32	0.61	3.47	27.88	0.81	2.70	0.39	2.47	0.36
	3H-2, 100-101	17.2	20.11	31.63	100.64	146.31	15.28	64.38	12.04	2.99	10.88	2.04	13.58	163.95	3.33	11.18	1.77	12.46	1.94
	3H-4, 100-101	20.2	23.11	32.25	16.40	22.95	3.39	14.95	2.99	0.69	2.57	0.46	2.79	19.67	0.60	1.99	0.27	1.85	0.22
	3H-6, 100-101	23.2	26.11	32.87	10.28	13.06	2.19	10.52	1.96	0.50	1.80	0.34	1.97	13.90	0.45	1.38	0.19	1.17	0.17
	4H-3, 75-76	27.95	31.21	34.36	21.93	24.38	4.30	19.53	3.74	1.00	3.32	0.60	3.84	29.30	0.90	2.86	0.42	2.52	0.42
	4H-5, 75-76	30.95	34.21	35.33	200.92	228.85	36.56	147.59	28.67	7.99	27.57	5.09	31.04	294.43	7.48	24.79	3.64	25.17	3.82
	4H-7, 65-66	33.85	37.11	35.95	13.75	10.07	2.94	14.16	2.84	0.75	2.52	0.49	2.85	22.14	0.69	2.08	0.26	1.79	0.26
	5H-2, 75-76	35.95	41.2	36.34	8.14	7.87	1.72	7.72	1.68	0.43	1.61	0.27	1.66	12.24	0.39	1.24	0.15	0.99	0.14
	5H-4, 75-76	38.95	44.2	36.87	7.30	7.88	1.58	6.76	1.42	0.43	1.42	0.28	1.81	12.48	0.37	1.11	0.16	1.02	0.16
	5H-6, 75-76	41.95	47.2	37.32	13.61	9.70	2.58	12.06	2.41	0.66	2.49	0.45	2.79	26.68	0.66	2.35	0.34	1.96	0.30
	6H-1, 75-76	43.95	51.11	37.96	11.91	10.04	2.58	11.94	2.46	0.68	2.54	0.46	2.85	22.15	0.65	2.14	0.28	1.81	0.29
	6H-3, 75-76	46.95	54.11	38.51	8.33	9.18	1.78	8.01	1.68	0.47	1.66	0.28	1.83	13.35	0.41	1.34	0.17	1.09	0.17
	6H-5, 75-76	49.95	57.11	38.83	10.00	5.73	1.56	6.85	1.38	0.37	1.29	0.24	1.47	10.56	0.31	1.05	0.14	0.86	0.13
	6H-7, 30-31	52	59.16	39.02	13.05	7.98	1.91	8.40	1.67	0.53	1.97	0.37	2.22	16.55	0.52	1.59	0.22	1.34	0.20
	7H-2, 75-76	54.95	64.76	39.52	6.99	5.06	1.04	4.33	0.86	0.26	0.76	0.15	0.90	6.60	0.21	0.62	0.08	0.57	0.08
	7H-4, 75-76	57.95	67.76	39.75	4.37	3.37	0.65	2.81	0.46	0.17	0.51	0.09	0.53	3.76	0.11	0.37	0.06	0.35	0.05
	7H-6, 75-76	60.95	70.76	39.96	6.08	4.04	1.00	3.39	0.80	0.24	0.78	0.14	0.82	6.63	0.17	0.62	0.09	0.65	0.11
	8H-1, 75-76	62.95	73.72	40.16	2.48	1.98	0.39	1.51	0.23	0.12	0.42	0.08	0.48	3.20	0.10	0.31	0.04	0.30	0.05
	8H-3, 75-76	65.95	76.72	40.30	3.42	2.40	0.48	2.13	0.41	0.14	0.49	0.08	0.52	3.35	0.11	0.41	0.05	0.33	0.04
	8H-5, 75-76	68.95	79.72	40.44	3.86	2.55	0.53	1.75	0.27	0.15	0.41	0.10	0.55	4.14	0.14	0.41	0.07	0.39	0.06
	8H-7, 40-41	71.6	82.37	40.57	5.70	2.42	0.75	2.81	0.53	0.17	0.54	0.08	0.52	3.28	0.10	0.29	0.03	0.25	0.04
	9H-3, 75-76	75.45	86.81	40.78	6.51	4.46	0.94	3.58	0.63	0.22	0.97	0.16	0.98	6.77	0.21	0.68	0.09	0.60	0.07
	9H-5, 75-76	78.45	89.81	40.92	8.94	3.18	1.09	4.24	0.91	0.31	1.15	0.20	1.11	8.04	0.23	0.77	0.09	0.60	0.08
	9H-7, 55-56	81.25	92.61	41.05	11.48	4.18	1.43	4.77	0.69	0.39	1.22	0.24	1.39	10.15	0.30	0.92	0.12	0.75	0.08

Table 3.6. Rare Earth Element Concentration Results of Site U1332 ODED Samples

	Core, section, interval	Depth (CSF)	Depth (CCSF)	Age (Ma) [GTS 2012]	La	Ce	Pr	Nd	Sm	Eu	Gd	Tb	Dy	Y	Ho	Er	Tm	Yb	Lu
Hole U1332A-																			
	6H-4, 75-76	47.15	52.65	29.73	11.98	19.13	2.35	9.56	1.97	0.47	1.61	0.29	1.79	13.02	0.41	1.26	0.19	1.11	0.18
	6H-6, 75-76	50.15	55.65	30.33	14.50	23.48	2.78	11.22	2.21	0.55	1.73	0.35	2.09	14.61	0.48	1.60	0.22	1.37	0.23
	7H-1, 75-76	52.15	59.9	31.15	18.44	23.57	3.56	14.94	3.02	0.80	2.72	0.53	3.52	29.57	0.82	2.69	0.36	2.39	0.39
	7H-3, 75-76	55.15	62.9	31.55	11.53	19.26	2.41	9.47	2.01	0.38	1.74	0.35	2.30	15.67	0.49	1.66	0.24	1.51	0.25
	7H-5, 75-76	58.15	65.9	31.95	8.13	12.77	1.62	6.99	1.38	0.35	1.11	0.21	1.43	9.89	0.32	1.10	0.14	0.87	0.14
	7H-7, 35-36	60.75	68.5	32.29	5.01	7.74	1.05	4.24	0.86	0.24	0.77	0.16	0.98	6.81	0.22	0.73	0.10	0.63	0.10
	8H-3, 75-76	64.65	72	32.76	2.26	3.48	0.50	2.21	0.50	0.14	0.42	0.07	0.47	3.40	0.10	0.35	0.04	0.31	0.04
	8H-5, 75-76	67.65	75	33.16	5.99	9.18	1.25	5.33	1.08	0.30	1.03	0.20	1.29	8.95	0.28	0.89	0.14	0.86	0.15
	8H-7, 35-36	70.25	77.6	33.64	10.55	15.20	2.15	9.33	2.01	0.52	1.68	0.31	2.06	14.39	0.44	1.51	0.20	1.31	0.21
	9H-2, 75-76	72.65	75.28	33.21	7.94	9.73	1.71	7.21	1.59	0.46	1.40	0.27	1.80	12.21	0.36	1.20	0.18	1.06	0.17
	9H-4, 75-76	75.65	78.28	33.80	10.84	15.13	2.39	10.09	2.38	0.62	2.05	0.41	2.40	16.16	0.50	1.69	0.25	1.47	0.23
	9H-6, 75-76	78.65	81.28	34.73	6.41	9.04	1.45	6.47	1.45	0.42	1.35	0.25	1.52	10.37	0.35	1.12	0.16	1.01	0.15
	9H-7, 35-36	79.75	82.38	35.06	5.97	8.43	1.40	5.98	1.33	0.39	1.25	0.23	1.53	10.49	0.35	1.09	0.16	0.90	0.14
	10H-1, 85-86	80.75	84.05	35.51	6.69	9.91	1.47	6.21	1.38	0.38	1.24	0.24	1.55	11.01	0.37	1.27	0.17	1.10	0.16
	10H-3, 75-76	83.65	86.95	36.22	8.01	9.17	1.75	7.92	1.78	0.51	1.48	0.30	2.02	13.12	0.40	1.39	0.20	1.16	0.16
	10H-5, 75-76	86.65	89.95	36.83	5.77	5.44	1.33	5.76	1.40	0.40	1.39	0.24	1.60	10.87	0.34	1.13	0.15	0.91	0.14
	10H-7, 40-41	89.3	92.6	37.26	2.91	3.24	0.68	3.06	0.74	0.21	0.68	0.12	0.79	5.37	0.16	0.54	0.08	0.46	0.08
	11H-3, 75-76	93.15	96.53	37.92	8.84	7.13	1.95	8.77	1.98	0.62	1.98	0.37	2.31	17.07	0.54	1.67	0.22	1.45	0.19
	11H-5, 75-76	96.15	99.53	38.53	7.59	5.27	1.24	5.29	1.24	0.33	1.10	0.22	1.33	8.63	0.28	0.93	0.11	0.78	0.11
	12H-2, 75-76	101.15	107.37	39.53	4.29	2.61	0.58	2.54	0.51	0.16	0.49	0.09	0.54	4.15	0.12	0.43	0.07	0.44	0.07
	12H-4, 75-76	104.15	110.37	39.88	3.83	3.18	0.61	2.41	0.44	0.15	0.38	0.08	0.44	2.88	0.09	0.30	0.04	0.30	0.05
	12H-6, 65-66	107.05	113.27	40.20	2.01	1.39	0.29	1.21	0.20	0.08	0.19	0.04	0.27	1.68	0.06	0.19	0.03	0.19	0.03
	13H-1, 75-76	109.15	117.77	40.54	2.70	1.57	0.40	1.60	0.32	0.11	0.32	0.06	0.32	2.07	0.07	0.23	0.03	0.16	0.03
	13H-3, 75-76	112.15	120.77	40.77	4.38	1.93	0.58	2.56	0.68	0.24	0.85	0.15	0.95	7.24	0.21	0.76	0.10	0.69	0.10
	13H-5, 75-76	115.15	123.77	41.00	6.79	2.67	0.91	3.37	0.71	0.27	0.78	0.13	0.86	5.67	0.20	0.56	0.09	0.41	0.06
	13H-7, 65-66	118.05	126.67	41.23	5.23	2.31	0.78	3.36	0.73	0.19	0.75	0.14	0.84	5.48	0.17	0.63	0.08	0.51	0.07
	14H-3, 75-76	121.65	134.15	41.92	3.74	1.66	0.59	2.40	0.53	0.18	0.48	0.10	0.60	3.77	0.13	0.41	0.04	0.32	0.04

Table 3.7. Rare Earth Element Concentration Results of Site U1333 ODED Samples

	Core, section, interval	Depth (CSF)	Depth (CCSF)	Age (Ma) [GTS 2012]	La	Ce	Pr	Nd	Sm	Eu	Gd	Tb	Dy	Y	Ho	Er	Tm	Yb	Lu
Hole U1333A-																			
	9H-7, 55-56	85.55	101.28	30.92	6.93	11.25	1.46	6.62	1.45	0.34	1.20	0.23	1.42	10.08	0.34	1.01	0.17	0.97	0.14
	10H-2, 75-76	87.75	105.11	31.25	4.06	6.06	0.84	4.12	0.82	0.24	0.76	0.13	0.91	6.38	0.18	0.57	0.12	0.56	0.08
	10H-4, 75-76	90.75	108.11	31.50	2.34	3.82	0.42	2.18	0.65	0.09	0.31	0.06	0.47	3.24	0.11	0.38	0.06	0.41	0.05
	10H-6, 75-76	93.75	111.11	31.75	0.93	1.61	0.22	1.08	0.22	0.08	0.16	0.03	0.20	1.33	0.05	0.12	0.02	0.12	0.02
	11X-1, 75-76	95.75	114.47	32.03	2.31	3.31	0.49	2.27	0.45	0.22	0.39	0.09	0.53	4.39	0.14	0.32	0.07	0.36	0.07
	11X-3, 75-76	98.75	117.47	32.29	25.40	31.50	5.05	21.65	4.31	1.18	3.80	0.70	4.67	34.43	1.02	3.14	0.52	3.20	0.46
	12X-1, 105-106	101.75	121.2	32.60	1.30	2.63	0.33	1.65	0.32	0.11	0.28	0.06	0.34	2.34	0.07	0.24	0.04	0.24	0.03
	12X-3, 75-76	104.45	123.9	32.82	1.44	2.08	0.34	1.38	0.37	0.11	0.28	0.05	0.34	2.37	0.07	0.21	0.04	0.23	0.03
	12X-5, 75-76	107.45	126.9	33.08	12.59	2.95	2.33	9.56	1.49	0.42	1.30	0.26	1.71	14.12	0.39	1.18	0.19	0.98	0.16
	13X-2, 60-61	112.4	133.75	34.02	6.77	7.37	1.30	5.78	1.21	0.33	1.08	0.23	1.30	9.06	0.26	0.82	0.15	0.81	0.13
	13X-4, 75-76	115.55	136.9	35.18	18.56	11.93	2.55	10.38	2.10	0.66	2.15	0.41	2.90	33.09	0.65	2.10	0.35	1.87	0.27
	13X-6, 75-76	118.55	139.9	36.18	4.20	4.61	0.91	4.13	0.86	0.27	0.80	0.15	0.98	6.64	0.20	0.64	0.10	0.60	0.08
	14X-1, 75-76	120.75	142.36	36.53	3.00	2.85	0.70	3.35	0.69	0.20	0.67	0.12	0.75	5.45	0.16	0.49	0.08	0.45	0.07
	14X-3, 75-76	123.75	145.36	36.99	2.80	2.48	0.67	3.08	0.76	0.19	0.77	0.12	0.73	5.38	0.16	0.51	0.09	0.46	0.07
	14X-5, 75-76	126.75	148.36	37.52	4.54	3.15	1.03	5.01	1.06	0.35	1.20	0.21	1.31	9.36	0.29	0.87	0.13	0.78	0.11
	14X-7, 30-31	129.3	150.91	37.94	4.85	3.84	1.11	5.22	1.17	0.37	1.13	0.20	1.42	9.73	0.29	0.90	0.14	0.87	0.11
	15X-2, 75-76	131.85	156.55	38.76	7.21	3.31	1.05	4.73	0.98	0.28	0.86	0.15	0.93	5.99	0.20	0.62	0.08	0.51	0.07
	15X-4, 75-76	134.85	159.55	39.11	8.28	3.87	1.09	4.74	1.00	0.26	0.91	0.16	1.04	6.95	0.21	0.67	0.12	0.51	0.08
	15X-6, 75-76	137.85	162.55	39.45	4.04	2.09	0.58	2.50	0.52	0.16	0.52	0.09	0.54	4.07	0.12	0.37	0.06	0.39	0.05
	16X-2, 75-76	141.45	167.45	40.13	2.83	1.54	0.48	1.95	0.49	0.15	0.40	0.07	0.48	2.89	0.10	0.28	0.04	0.28	0.04
	16X-4, 75-76	144.45	170.45	40.39	2.45	1.30	0.41	1.59	0.38	0.12	0.30	0.07	0.43	2.40	0.08	0.25	0.04	0.23	0.03
	16X-6, 75-76	147.45	173.45	40.64	3.04	1.22	0.38	1.53	0.33	0.12	0.28	0.05	0.37	2.30	0.07	0.22	0.03	0.17	0.03
	17X-1, 75-76	149.55	177.75	41.01	6.03	2.26	0.94	4.11	0.85	0.29	0.86	0.15	0.96	6.72	0.20	0.59	0.10	0.51	0.07
	17X-3, 75-76	152.55	180.75	41.32	5.94	1.99	0.82	3.52	0.80	0.25	0.80	0.13	0.88	5.78	0.17	0.51	0.07	0.44	0.05
	17X-5, 75-76	155.55	183.75	41.93	3.89	1.36	0.55	2.29	0.45	0.17	0.49	0.09	0.58	3.76	0.13	0.37	0.06	0.33	0.04

Table 3.8. Rare Earth Element Concentration Results of Terrigenous Extraction Residues

	Core, section, interval	Depth (CSF)	Depth (CCSF)	Age (Ma) [GTS 2012]	La	Ce	Pr	Nd	Sm	Eu	Gd	Tb	Dy	Y	Ho	Er	Tm	Yb	Lu
Terrigenous Ext. from Hole U1332A																			
	8H-3, 75-76	64.65	72.00	32.76	10.90	24.47	2.18	9.05	1.70	0.45	1.45	0.30	1.79	13.01	0.42	1.39	0.22	1.32	0.24
	8H-4, 75-76	66.15	73.50	32.96	16.65	30.75	3.43	14.82	2.53	0.58	2.64	0.44	2.87	17.91	0.63	2.08	0.30	2.26	0.31
	9H-1, 75-76	71.15	73.78	33.00	22.80	45.89	4.79	20.08	3.76	0.65	3.22	0.58	3.55	23.12	0.73	2.32	0.36	2.18	0.37
	8H-5, 75-76	67.65	75.00	33.16	24.30	54.47	4.66	18.29	3.39	0.79	2.91	0.56	3.51	27.76	0.78	2.52	0.43	2.68	0.41
	9H-2, 75-76	72.65	75.28	33.21	13.73	26.55	2.77	11.50	2.10	0.62	1.84	0.39	2.75	18.51	0.58	1.81	0.31	1.86	0.28
	8H-6, 75-76	69.15	76.50	33.43	12.46	26.34	2.69	11.49	2.45	0.69	2.36	0.55	3.56	26.76	0.82	2.77	0.48	2.97	0.46
	9H-3, 75-76	74.15	76.78	33.48	17.69	35.11	3.61	14.24	3.05	0.91	2.98	0.55	3.93	30.70	0.83	2.93	0.47	2.79	0.44
	8H-7, 35-36	70.25	77.60	33.64	11.93	23.39	2.36	9.87	2.20	0.71	2.35	0.49	3.50	26.15	0.77	2.41	0.39	2.49	0.39
	9H-4, 75-76	75.65	78.28	33.80	312.22	323.42	48.60	175.84	31.27	8.17	27.57	5.36	34.49	370.66	7.27	24.09	4.45	28.33	4.44
	9H-5, 75-76	77.15	79.78	34.26	10.51	21.85	2.13	8.76	1.66	0.48	1.27	0.26	1.70	11.49	0.37	1.21	0.20	1.18	0.20
	9H-6, 75-76	78.65	81.28	34.73	9.61	18.14	1.86	7.17	1.61	0.41	0.98	0.25	1.42	10.88	0.35	1.34	0.22	1.58	0.24
	9H-7, 35-36	79.75	82.38	35.06	20.88	35.63	4.45	16.82	3.41	0.92	3.18	0.60	3.64	24.59	0.79	2.88	0.44	2.94	0.39
	10H-1, 85-86	80.75	84.05	35.51	10.61	20.25	2.17	9.29	1.70	0.50	1.42	0.27	1.77	12.53	0.39	1.25	0.22	1.51	0.22
	10H-2, 75-76	82.15	85.45	35.86	32.81	33.74	4.16	14.62	2.60	0.76	2.67	0.54	3.84	62.04	0.89	3.20	0.64	4.15	0.67
	10H-3, 75-76	83.65	86.95	36.22	10.23	16.04	2.09	8.85	1.64	0.50	1.42	0.28	1.80	12.39	0.38	1.28	0.23	1.32	0.18
	10H-4, 75-76	85.15	88.45	36.54	8.47	14.43	1.83	7.46	1.29	0.41	1.29	0.25	1.52	10.24	0.32	1.03	0.20	1.04	0.17
	10H-5, 75-76	86.65	89.95	36.83	17.96	16.98	3.83	15.03	2.90	0.82	2.41	0.50	3.02	20.33	0.63	1.92	0.33	1.95	0.28
	10H-6, 75-76	88.15	91.45	37.08	7.34	12.50	1.42	6.06	1.13	0.34	1.02	0.20	1.36	9.39	0.28	0.95	0.16	1.00	0.17
	10H-7, 40-41	89.30	92.60	37.26	6.17	13.11	1.22	4.90	0.95	0.32	0.82	0.16	1.14	7.79	0.24	0.71	0.14	0.87	0.12
	11H-2, 75-76	91.65	95.03	37.63	11.92	13.44	2.48	10.11	1.94	0.60	1.69	0.33	2.19	16.27	0.47	1.60	0.26	1.58	0.23
	11H-3, 75-76	93.15	96.53	37.92	13.26	12.68	2.91	12.15	2.37	0.69	2.23	0.45	2.82	19.30	0.57	1.78	0.31	1.78	0.27
	11H-4, 75-76	94.65	98.03	38.21	8.95	11.45	1.84	7.56	1.53	0.46	1.33	0.27	1.79	11.76	0.36	1.11	0.22	1.24	0.18
	11H-5, 75-76	96.15	99.53	38.53	11.33	11.78	2.53	10.55	2.09	0.63	1.85	0.37	2.40	15.98	0.47	1.47	0.28	1.54	0.24
	11H-6, 75-76	97.65	101.03	38.75	10.85	11.58	2.44	9.98	2.04	0.58	1.88	0.37	2.33	15.94	0.50	1.47	0.26	1.61	0.22

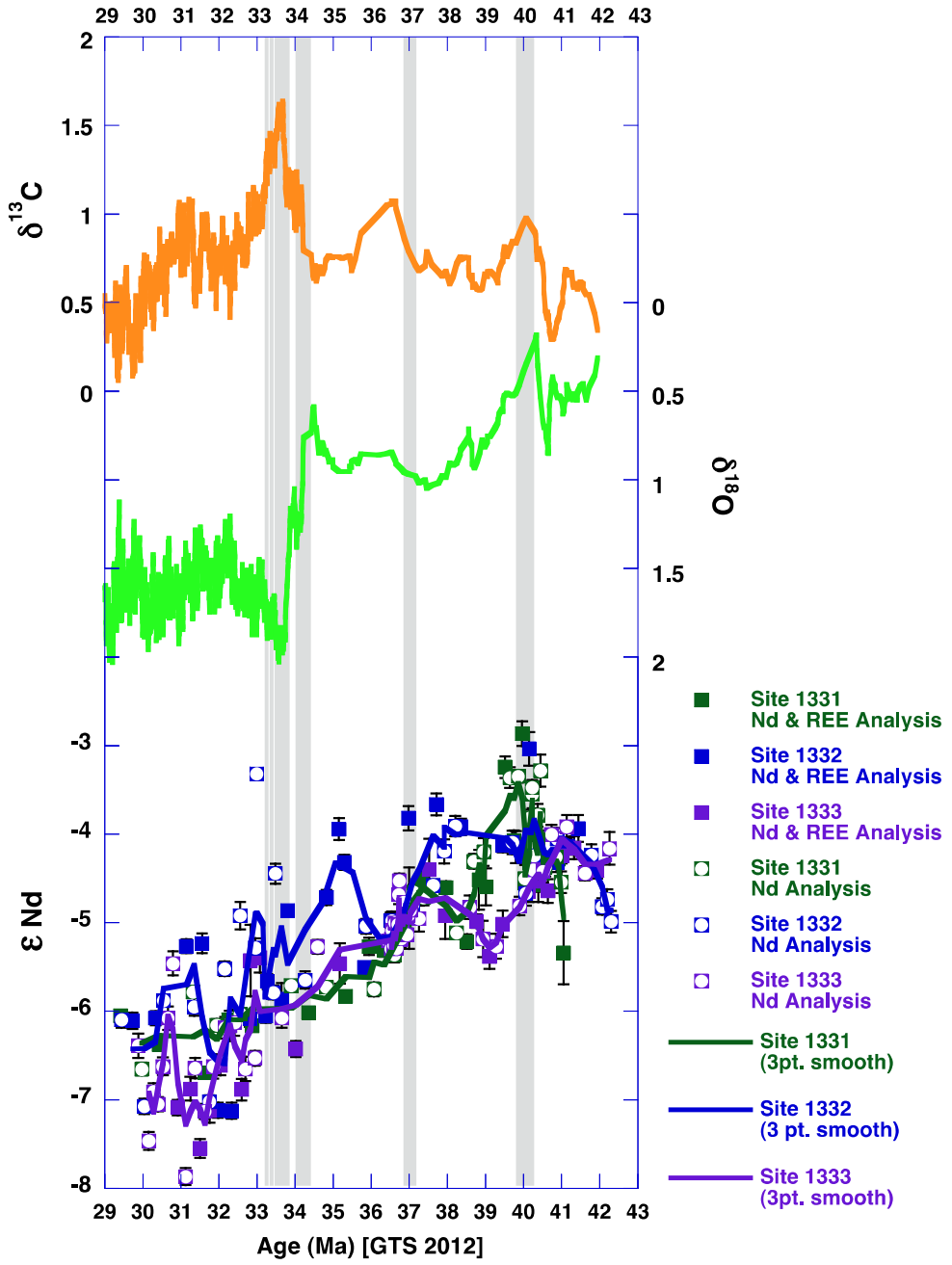

Figure 3.1. Measured ε_{Nd} values of samples with 3 point smoothed lines to show trends, relative to $\delta^{13}C$ and $\delta^{18}O$ (Palike et. al., 2006) during the period of study. Gray lines highlight the MECO, Priabonian/Bartonian boundary, and the EOT, periods of interest due to changes in global thermal gradients. Note, empty squares show samples that were only measured for Nd isotopic analysis, whereas colored squares were measured for Nd isotopic analysis and REE elemental analysis. Error bars represent two standard error plotted for each Nd measurement.

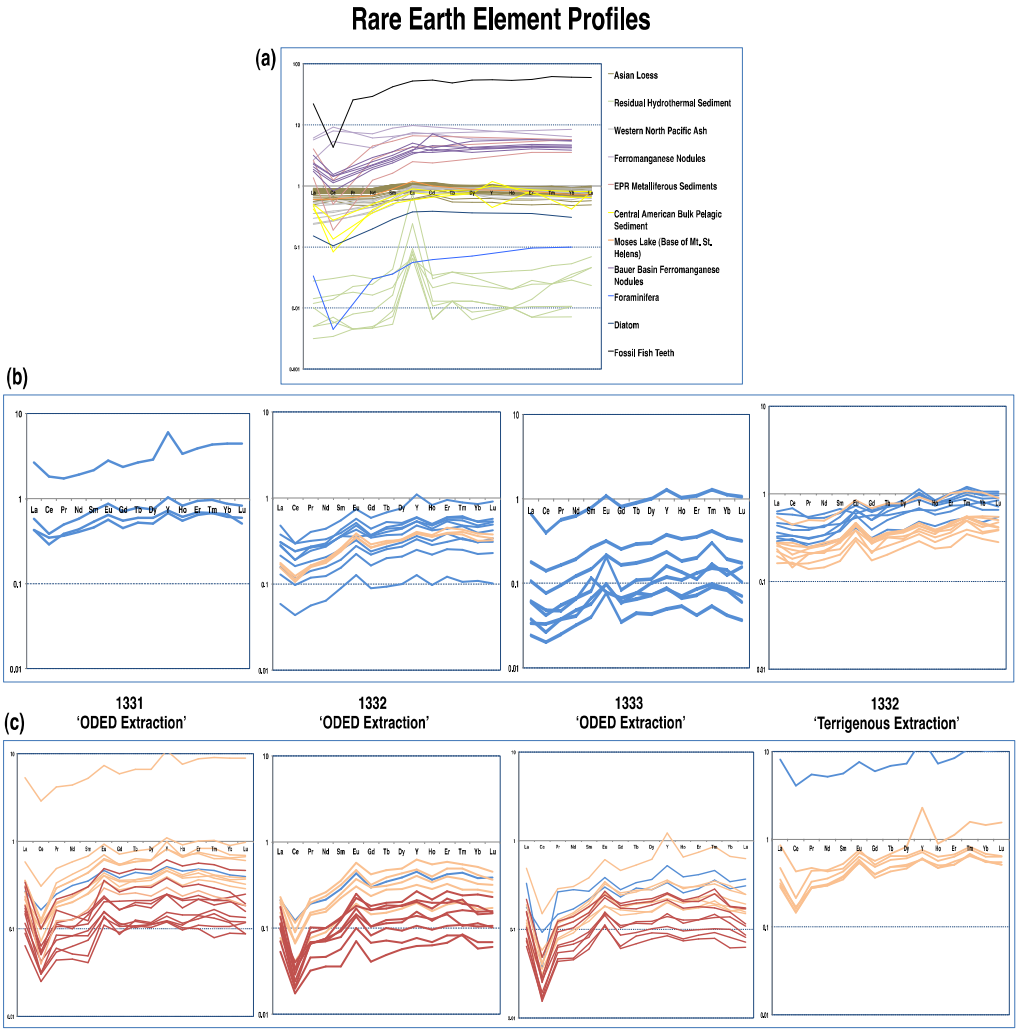

Figure 3.2. Post Achaean Australian Shale (PAAS) normalized REE profile patterns from sample sites; sample resolution of elemental analysis is ~480-500 ka, double that of Nd isotopic analysis. a) Reference REE patterns, Asian loess (Jahn et. al., 2001), residual hydrothermal sediment (Severmann et. al., 2004), western North Pacific ash (Bailey, 1993), ferromanganese nodules (Elderfield & Greaves, 1981), East Pacific Rise (EPR) metalliferous sediments (Elderfield & Greaves, 1981), Central American bulk pelagic sediment (Plank & Langmuir, 1998), Moses Lake (Nakai, 1993), Bauer Basin ferromanganese nodules (Elderfield & Greaves, 1981), foraminifera (Elderfield et. al., 1981), diatom (Elderfield et. al., 1981), and fossil fish tooth (Exp. 320 U1332A 9H-4, 75-76) (Scher, In Prep.). b) Sample REE profile patterns that have a negative cerium anomaly greater than 0.6 (less of a negative cerium anomaly) [$Ce/Ce^* = (3Ce_{(n)})/(2La_{(n)} + Nd_{(n)})$] (Subscript (n) are PAAS normalized values). c) Sample REE profile patterns that have a negative cerium anomaly less than 0.6 (greater negative cerium anomaly). Colors bin ages of samples: Blue (30-34 Ma), Orange (34.1-38 Ma), and Red (38.1-42 Ma). Note the prominent negative cerium anomaly indicates a seawater source.

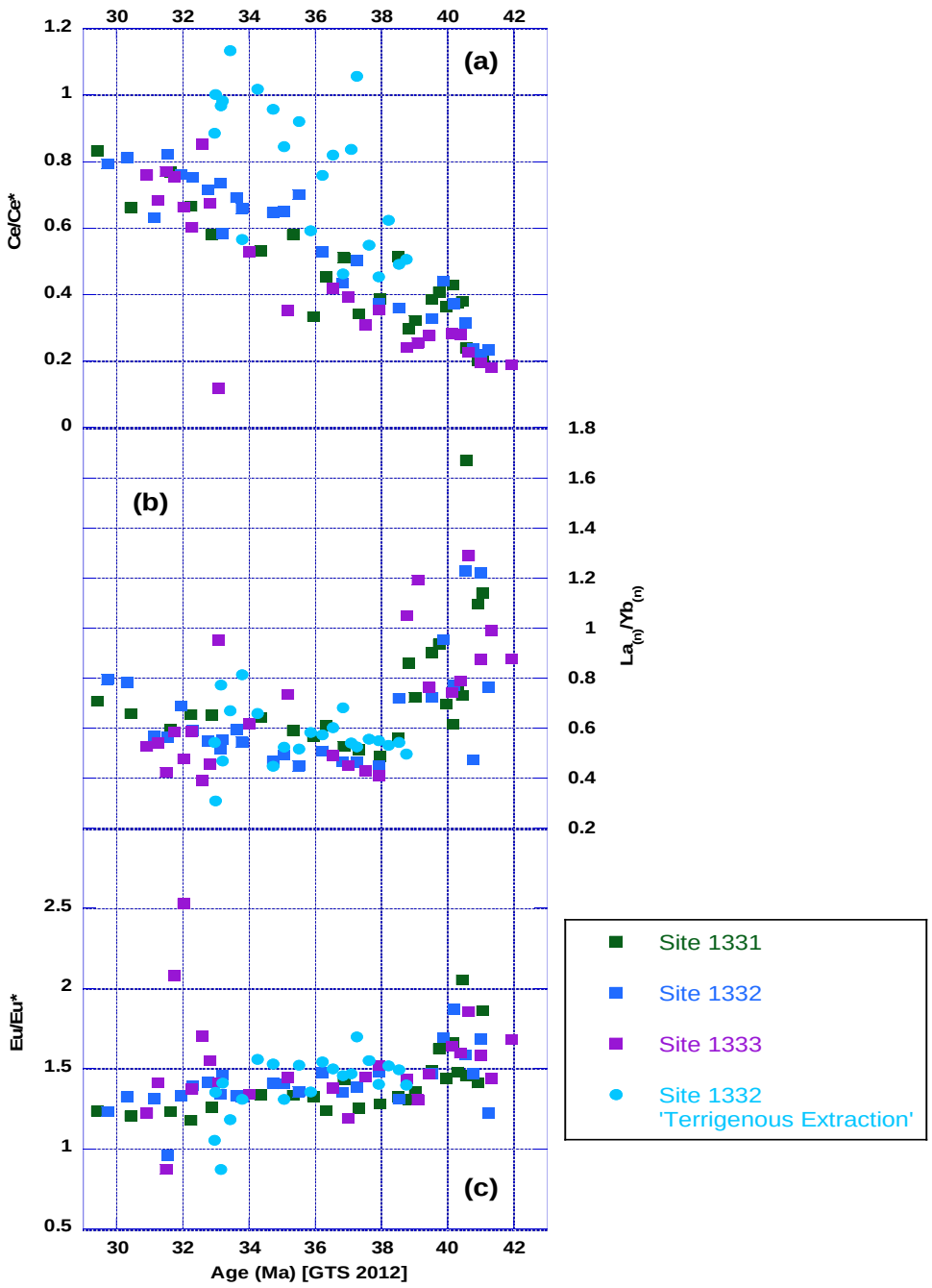

Figure 3.3. Elemental results of samples. a) Cerium, Ce/Ce*, anomaly for samples. b) Ratio between light rare earth elements (LREE): heavy rare earth elements (HREE) in the form of $La_{(n)}/Yb_{(n)}$. c) Europium anomaly, Eu/Eu*, where [Eu/Eu* = $(2Eu_{(n)})/(Sm_{(n)} + Gd_{(n)})$]; all with respect to period of interest.

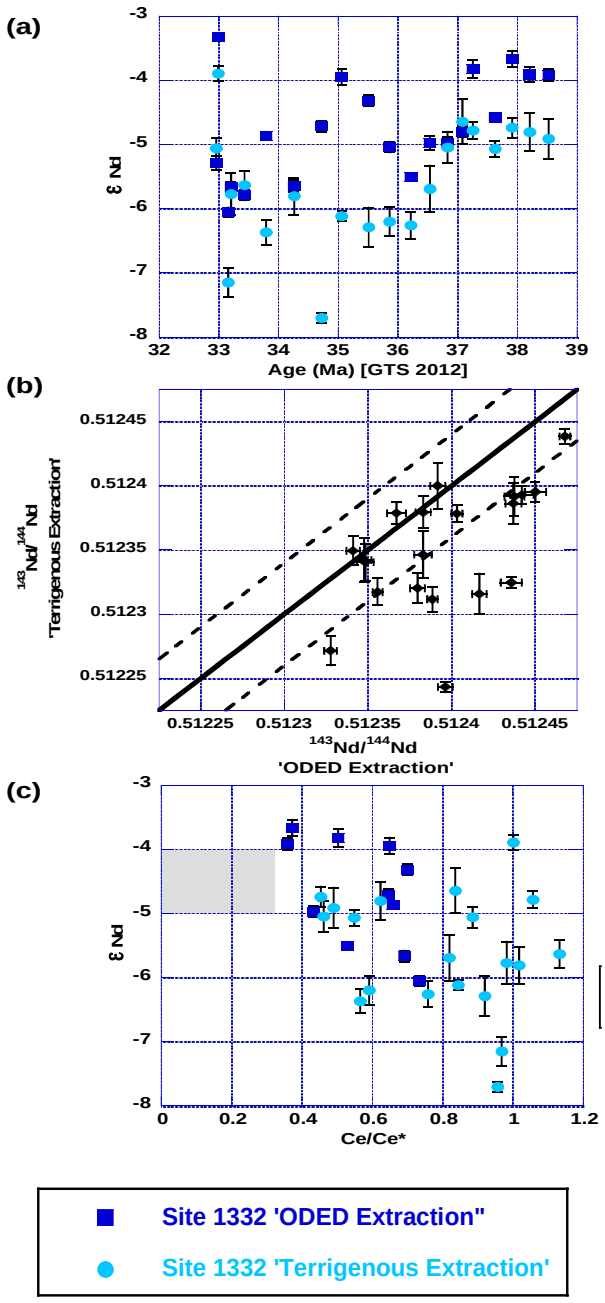

Figure 3.4. Comparison between different sequential chemical leaches of samples from Site U1332 to explore seawater signal and/or other possible contaminates to the ODED fraction. a) ε_{Nd} for both extractions. b) $^{143}Nd/^{144}Nd$ 1:1 plot, solid black line indicates the 1:1 line and dotted black lines represent two standard deviation (2σ= 0.00002), 2σerror envelopes, from the 1:1 line. c) ε_{Nd} against Ce/Ce* mixing line; gray shaded area signifies seawater values from fossil fish teeth measurements during interval of study (Scher, In Prep.). Error bars represent two standard error plotted for each Nd measurement.

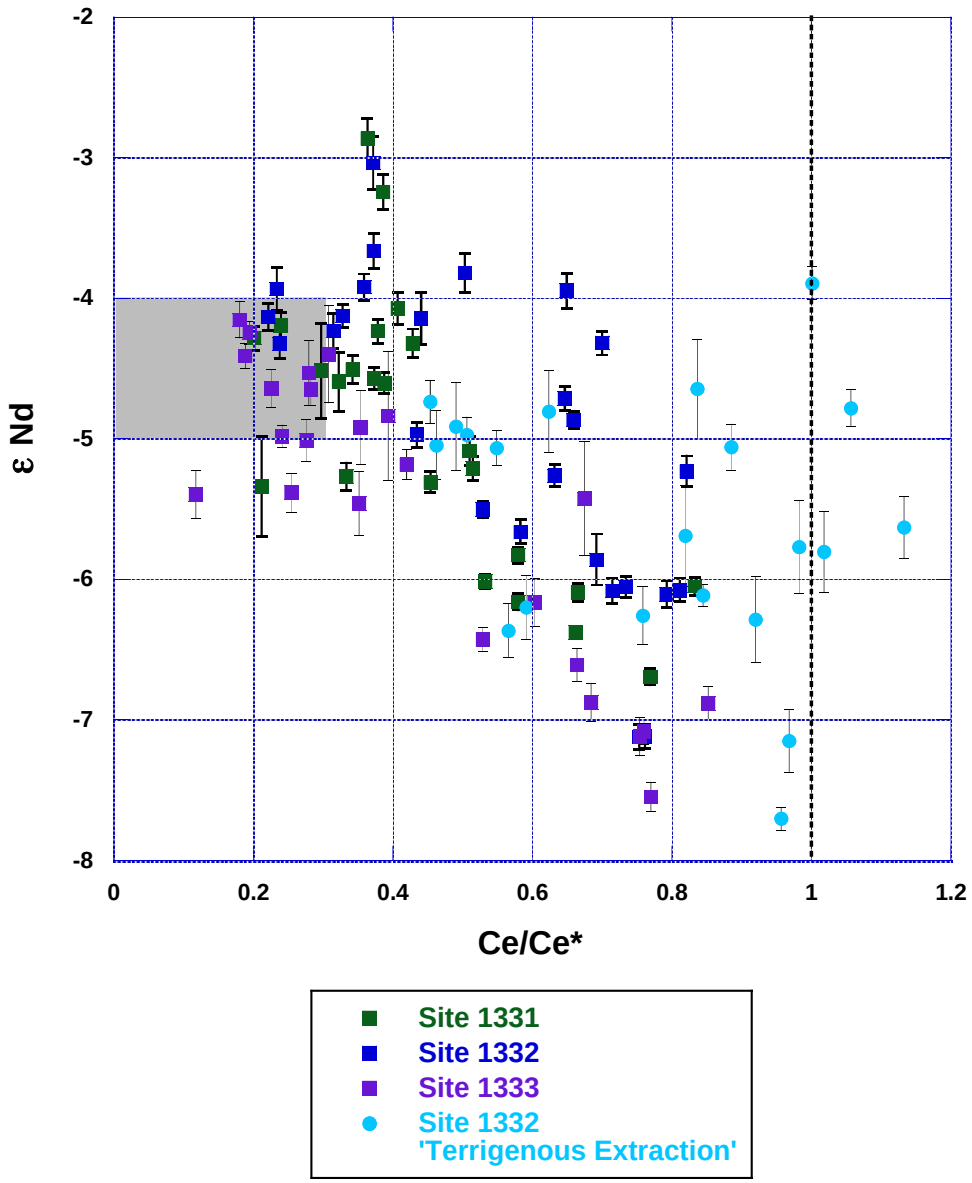

Figure 3.5. Relationship between ε_{Nd} and negative Ce/Ce* anomaly for samples with isotopic and elemental analysis. Dotted line highlights Ce/Ce* =1, no cerium anomaly; gray shaded area signifies seawater values from fossil fish teeth measurements during interval of study (Scher, In Prep.). Error bars represent two standard error plotted for each Nd measurement.

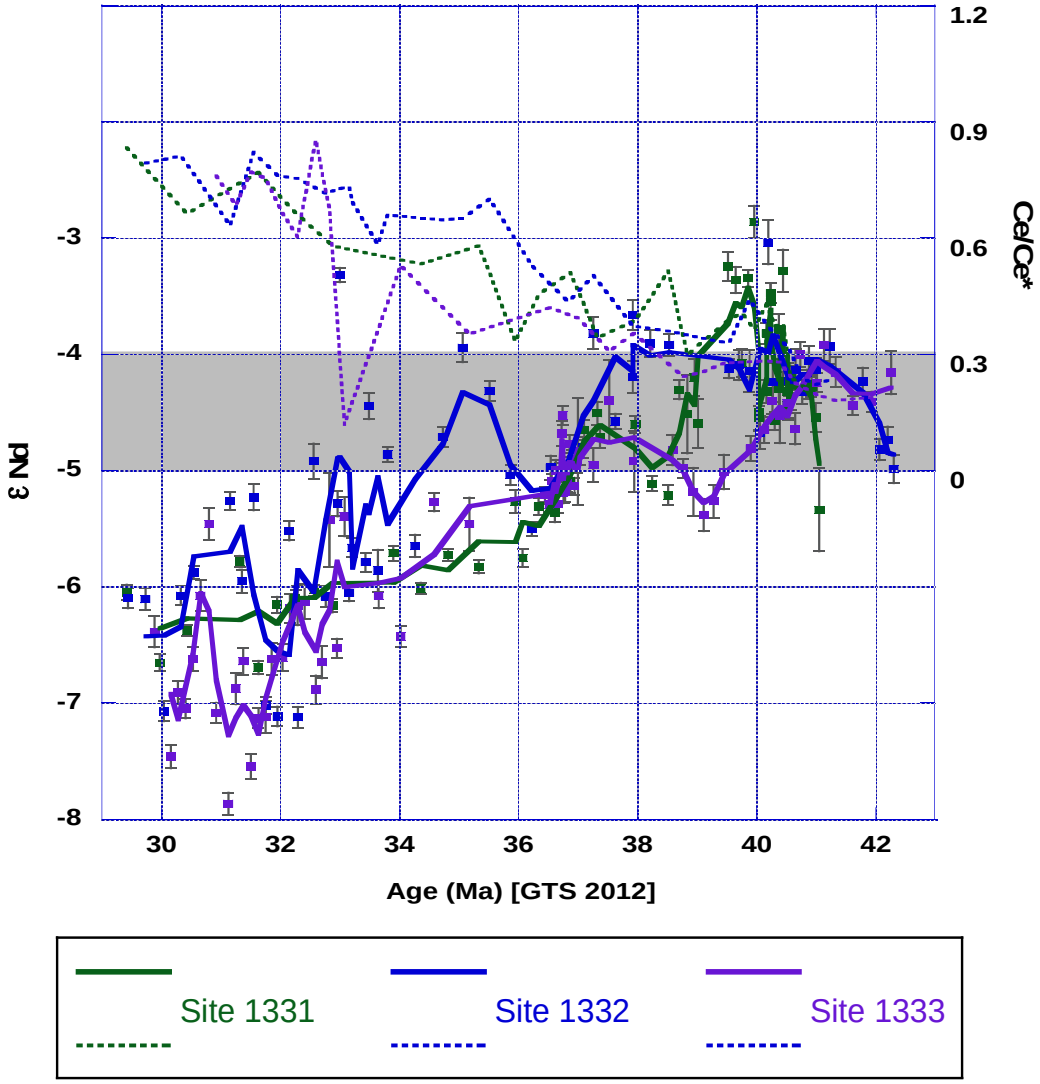

Figure 3.6. ε_{Nd} values with 3 pt. smoothed line and Ce/Ce* anomaly plotted against age for each sample, using sample ages calculated from GTS 2012 age model (Westerhold et. al., 2013). Gray box delineates seawater conditions during period of interest from fossil fish teeth record from same sites (Scher, In Prep.)

CHAPTER 4

DISCUSSION

The change in ε_{Nd} values over the course of the study, from more radiogenic (~-4) around 42 Ma to less radiogenic values (~-8) around ~30 Ma, can be explained by an increased fraction of material derived from old continental crust. However, all of the ODED samples have a negative cerium anomaly, though increasingly less pronounced as samples progressively get younger, which is attributed to a biasing geochemical seawater signal assumed to be of biogenic and/or authigenic origin. The relationship between ODED ε_{Nd} values and negative cerium anomalies (Figure 3.4c and 3.5) are considered a mixing line between endmembers of a seawater signal, signified by fossil fish teeth, and a projected less radiogenic, older continental signature, providing temporal insight into possible sources and the conditions in which it was deposited over the interval of study. Therefore we explore two main possible controls on the ODED, either a change in source, or a change in the sedimentary phases in the cores due to the spatial position relative to the high productivity zone and/or the depth of the CCD.

4.1 A Change in Source

When taking into account solely the ε_{Nd} data, ε_{Nd} values appear to change from a more radiogenic source, like that of Central (ε_{Nd} = ~-1 to 4) and South

America, (ε_{Nd} = ~-4) (Jones et. al., 2000; Nakai et. al., 1993; Pettke et. al., 2002; Stancin et. al., 2006; Xie & Marcantonio, 2012) to an older more continental source like that of Asian loess (ε_{Nd} = ~-10) (Nakai et. al., 1993; Grousset & Biscaye, 2005; Stancin et. al., 2006; Xie & Marcantonio, 2012), and Australian dust and Saharan dust suggested by models but are not supported by any geochemical data (ε_{Nd} = ~-15) (Luo et. al., 2003; Grousset & Biscaye, 2005; Leduc et. al., 2009; Maher et. al., 2010; Xie & Marcantonio, 2012). Due to the sites spatially being all north of the approximate center of the reconstructed Eocene equatorial divergence portrayed in Moore et. al., (2004); if assumed that the ITCZ is linked to the equatorial biogenic mound and the equatorial divergence, then the reigning atmospheric convection cells would be that of the northern hemisphere. In turn the surface trade winds would be the northeasterly trades rather than the southeasterly trades of the equatorial bracketing Hadley cells, and the westerlies of the latitudinally adjacent Ferrel cell.

Thus, when the thermal gradient was low, during the MECO, the more radiogenic ε_{Nd} value of -3 may be due to a weakening in the wind patterns, the northeasterly trades, bringing more proximal sources of South America, due to a decreasing contribution of Central American sources, to the sites. As glacial regimes prevail and the thermal gradient increases around 37 Ma, the sites appear to be influenced by two sources, younger and older continental ε_{Nd} values; this may be explained by the mixing between that of South America (ε_{Nd} = ~-4) and Asian loess (ε_{Nd} = ~-10), implying the influence of both the westerlies and the northeasterly trades. Furthermore during the interval when the thermal

gradient was steepest, in the early Oligocene, the westerlies appear to intensify shown by the least radiogenic and oldest continental ε_{Nd} signatures. This is a plausible explanation whereby the aeolian influence from the westerlies was more important to the study sites compared to the northerlestly trades, for the westerlies have been argued to reach as far as 118^{o}W and 5^{o}N in times of increased wind intensities (Jones et. al., 2000).

However, the interpretation is not as straightforward when the REE profiles are taken into account. The aforementioned explanation does not corroborate with negative cerium anomalies (Ce/Ce* < 0.6) present in all of the ODED samples until ~36-37 Ma, as continental sources such as South and Central America do not display a negative cerium anomaly. The negative cerium anomalies associated with the ODED extraction are similar to that of known recorders of seawater, (see reference profiles in Figure 3.2a) that of biogenic and authigenic sources. Moreover during 42 – 39 Ma, spanning the MECO, there is a feature present in the cerium and europium anomalies and in the $La_{(n)}/Yb_{(n)}$ ratios that do not coincide with the straightforward approach of just the ε_{Nd} values. Consequently, another explanation would be that of a mixing between a biasing seawater signature and that of older continental sources, like that of the proposed Asian loess delivered by the westerlies during the periods of increased thermal gradient, after ~37 Ma. The cerium anomalies and $La_{(n)}/Yb_{(n)}$ ratios after this marked period during the MECO, are in support of the interpretation of mixing between a geochemical seawater signature and older continental source. This is shown by greater negative cerium anomalies, ~0.3, and low $La_{(n)}/Yb_{(n)}$

ratios, ~0.4, approximately that of fossil fish teeth since seawater is depleted in LREE (Toyoda et. al., 1990), temporally changing to cerium anomalies and $La_{(n)}/Yb_{(n)}$ values of ~0.8, closer to that of continental values of 1. Further justification of this conceptual mixture can be seen in Figure 3.6, when ε_{Nd} values and cerium anomalies of ODED samples trend away from the grayed region around ~36.5-37 Ma marked by the increase in thermal gradient at the Priabonian/Bartonian boundary, representing departure from a biasing geochemical seawater signature to an older continental source. A viable interpretation of the biogenic and/or authigenic seawater signature biasing the provenance data is a possible change in the sedimentary phases in the cores due to the spatial position relative to the high productivity zone and/or the depth of the CCD.

4.2 A Change in Sedimentary Phase

4.2.1 Relative to High Productivity Zone

Within 3^{o}N of the equatorial zone has been known to be dominated by biogenic sedimentation and is within the present day equatorial high-productivity zone (Erhardt et. al., 2013). This corresponds to the spatial distribution of high mass accumulation rates indicating a zone of high productivity and the relative position of the ancient equatorial divergence (Moore et. al., 2004). Also it has been shown by leaching experiments and microscopic observation, that high biological activity in the equatorial Pacific results in a high content of fish bone debris, carbonate fluorapatite and biogenic calcium phosphate, in the sediment

which causes a large negative Ce anomaly, recording ε_{Nd} signatures of seawater like that of fossil fish teeth (Toyoda et. al., 1990; Toyoda & Masuda, 1991). This signature decreases latitudinally with distance from the equator or distance from the biological productivity zone (Toyoda et. al., 1990), capturing the increased tropic dynamics caused by high productivity. When taken with respect to the backtracked paleolocations of the sites, spatially, this would mean Sites U1331 and U1332 pass through and exit the high biological productivity zone of 3^{o}N, whereas Site U1333 during the study stays within the bounds of 3^{o}N.

The point at which Sites U1331 and U1332 depart the bounds of 3^{o}N and the assumed high productivity zone, is around ~36.5-37 Ma, the same time when ODED ε_{Nd} values and cerium anomalies trend away from and start resembling less of a biasing seawater signal, Figure 4.1. Additionally just before Sites U1331 and U1332 leave 3^{o}N, ε_{Nd} values for the sites are tight agreement. This agrees with the assumption that if the sites are spatially bound in the same region, the sites will experience the same or similar productive conditions, most likely that of the equatorial biological productivity zone, or above the biogenic mound (Moore et. al., 2004). Though after this period, when the thermal gradient increases with the emplacement of high elevation glaciers on Antarctica, Sites U1331 and U1332, drift outside the bounds of the high productivity zone of 3^{o}N.

As the sites move north of 3^{o}N, the northern most site, Site U1331, ε_{Nd} values remain stable and trend less radiogenic, while Site U1332 and U1333 increase variability after that point. The trend of Site U1331 (Figure 4.1) agrees with the fact that productivity is higher on the equator and decreases with

increasing distance from the equator in the EEP (Goldberg & Arrhenius, 1958; Xie & Marcantonio, 2012). This shows that the site is gradually experiencing less radiogenic signatures, steadily mixing between a geochemical seawater signal and the less radiogenic signatures of older continental sources. Although the same cannot be said for the two most southern sites, Sites U1332 and U1333, where variability in ε_{Nd} values increases after that point. The variability in Site U1333 can be explained by it never leaving the high productivity zone of 3^{o}N during the duration of this study, whereas Site U1332 does leave 3^{o}N.

Therefore a possible explanation for Site U1332 experiencing variability after 3^{o}N is that as the thermal gradient increases after the Priabonian/Bartonian boundary to after the EOT, the wind intensities increase, thereby increasing equatorial upwelling delivering more nutrients, causing the biological productivity zone to increase in size (Moore et. al., 2004). Thus Site U1332 and Site U1333 may be mixing more than Site U1331 with a seawater signature and a less radiogenic continental source causing the increased variability, due to the possible increase in carbonate fluorapatite and biogenic calcium phosphate. The progressive bulging of the high productivity zone may be engulfing and influencing the sites at different rates, giving light to the possible spatial constraint of the high productivity zone and the change within the down core sedimentary phases of the sites.

However, if it is expected that, due to increasing the trophic dynamics, an increase of fossil fish bone debris is associated with periods of high productivity in the equatorial region, then the greatest influence of a biasing seawater signal

attributed to fish bone debris would be after the EOT. This is not the case, the greatest influence is during the MECO and progressively lessening to and after the EOT, when productivity would be at its highest. Moreover, to see the effect of fish bone debris, a couple of samples were leached with 5 mls of 2% HNO_3 for 45 minutes, an extra step to the terrigenous extraction. The cerium anomaly after the new leaching step was still present, changing from 0.96 & 0.96 to 0.82 & 1.18, respectively. This allows for the assumption that biogenic calcium phosphate and carbonate fluorapatite are not the only possible changes in sedimentary phase spatially relative to the high productivity zone. In the same light, a couple of terrigenous extracted samples were additionally leached with 2 mls of warm 2.5 M HCl for ~20 minutes, to see the influence of basaltic amorphous glasses, providing a similar result but in regards to a less positive europium anomaly, changing from 1.53 & 1.99 to 1.37 & 1.46, respectively. This would mean that there are other possible biogenic and/or authigenic remnants that may have not been targeted or fully extracted during the leaching procedures that are causing the ODED to be biased by seawater signatures. Other possible sedimentary phases that could cause a biasing seawater signature and would remain after the leaching procedures, though ever reaching, is that of marine barite, which has been found to be abundant within $<3^{o}$ of the equator due to the high productivity (Xie & Marcantonio, 2012), and authigenic smectite. But without mineral or grain analysis by means of scanning electron microscope (SEM) or X-ray diffraction (XRD), the compositional contents of the ODED and terrigenous extraction residues are unknown, making the exact

culprits that are biasing the ODED provenance signature unable to be pinpointed and are strictly conjecture. However, any evidence of an insufficient leach or biasing components not targeted by the chemical extractions opens the possibility for a biogenic and/or authigenic seawater signature. Therefore the applicability of either of the two sequential chemical extractions used in this study may not be justified in the high production regions of the equatorial Pacific.

4.2.2 Relative to Depth of CCD

Based on the discussion above, the biasing geochemical seawater signal observed in the ODED samples cannot solely be explained by the migration of the sites through the high productivity zone. Another cause of down core changes in sedimentary phases would be the preservation of the sedimentary phases in the core. The preservation of the sites is regulated by the CCD, which would change differently for each of the sites due to the different depths the sites were cored. Site U1331 is the most northern and deepest site, followed by Site U1332, next deepest, and Site U1333 is the shallowest (Figure 2.2).

During the MECO, when a transient rise in pCO_2 levels is thought to have occurred (Bohaty & Zachos, 2003), the CCD shoaled in response to these increased CO_2 levels (Figure 2.2), above the paleodepths of all of the sites, giving a possible explanation for the similar ε_{Nd} values of all of the sites. Also before and after the MECO, CAE-3 and CAE-4 occur with the presence of a deeper CCD, below all of the paleodepths for the sites, providing the same preservation conditions until ~38 Ma. After this point in time, ~38 Ma, all of the

sites do not experience the same preservation conditions until after the EOT with the exception of 4 temporally short sporadic fluctuations, one of note around ~37 Ma, when the CCD shoals above all of the sites, separating CAE-5, CAE-6, CAE-7, and the EOT. Even with these periodic CAEs, the CCD does not deepen enough to encapsulate all of the sites in the same preservation regime. It does though for Sites U1332 and U1333, where preservation is the greatest in Site U1333, being the shallowest and highest CAR, and Site U1332 is engrossed by the melodic rhythms of the shoaling and deepening of the CCD during this time period. The fluctuations of the CCD relative to the paleodepths of Sites U1332 and U1333 may be an explanation for the variability found in the ε_{Nd} values. This would agree with the fact that the most variability is associated with Site U1332, which is the most erratic in terms of constant or similar preservation relative to the other sites, due to its paleodepth 'walking the line' of the CCD. Also in support of the variability notion, Site U1331, experiences the most consistent preservation conditions, being such that it is below the CCD for most of the study, causing less variability associated with the ε_{Nd} values, due to the conditions not constantly fluctuating.

These observations concur with the previous observations that one possible source may be that of a biogenic seawater signature preserved by the CCD. And when taken with respect to the proposed increase of fossil fish debris as a main component in the sedimentary phase, during times of increased dissolution due to the CCD being shallower than that of the paleodepths of the sites, preservation of fossil fish debris, carbonate fluorapatite & biogenic calcium

phosphate, would decrease causing the debris to become more brittle and to fragment. By fragmenting, the probability of fossil fish debris in the <63 μm size fraction would increase, thereby being incorporated more into the ODED samples. Consequently the temporal regulation on sedimentary preservation of the CCD in concert with the spatial migration through high productivity zone may be feasible explanations for changes in the sedimentary phases that may be the cause of the biasing geochemical seawater signature.

4.3 Linkage to Climate States

Without definitive endmembers to evaluate the prevailing wind systems during the course of study, it is difficult to make strong correlations in regards to the climate states. However broad relationships can be observed. During the MECO the CCD was above all sites, the wind systems, assumed northeasterly trades appeared weakened, delivering more radiogenic ε_{Nd} values that appear from more proximal sources to the sites; this may be caused by low biologic productivity due to low thermal gradients, allowing a more radiogenic signature than seawater values to prevail at this time. Also the peaks observed spanning 42- 39 Ma, in the cerium anomalies, europium anomalies, and high $La_{(n)}/Yb_{(n)}$ ratios may be linked to a global signal regarding oxygen content in the oceans. Moebius et. al., (2014) reported a positive excursion in the negative cerium anomalies in fossil fish teeth from the Indian sector of the Southern Ocean during the MECO, indicative of a decrease in bottom-water oxygen content. If this is

true, then it is further support that the ODED is biased by a biogenic and/or authigenic seawater component.

As the thermal gradient progressively increases, emerging throughout the study is the period ~37 Ma. All sites were within 3^{o}N, ε_{Nd} values were in agreement, and all below the CCD. After this point in time, sites trended less radiogenic, possibly by the increased winds delivering an older continental source that began to dominate the mixture between the seawater sources as the increasing thermal gradient prevails, culminating with the EOT. At that time, after the EOT, the thermal gradient was at the maximum during this the interval of study, implying the greatest intensification in the wind patterns, as inferred by the observed older continental ε_{Nd} values, inducing the most upwelling, thereby sequestering more carbon by increased export production, and reducing atmospheric CO_2 (Scher & Martin, 2006). If this is so, then the notion of increased stratification, reduced upwelling rates, and assumed decrease in productivity in the EEP during the EOT (Miller et. al., 2009; Erhardt et. al., 2013) due to the penetration of cold nutrient depleted Southern Ocean bottom must be explored to see what forces, stratification or wind stress, delineates the upwelling conditions during these important global climactic states.

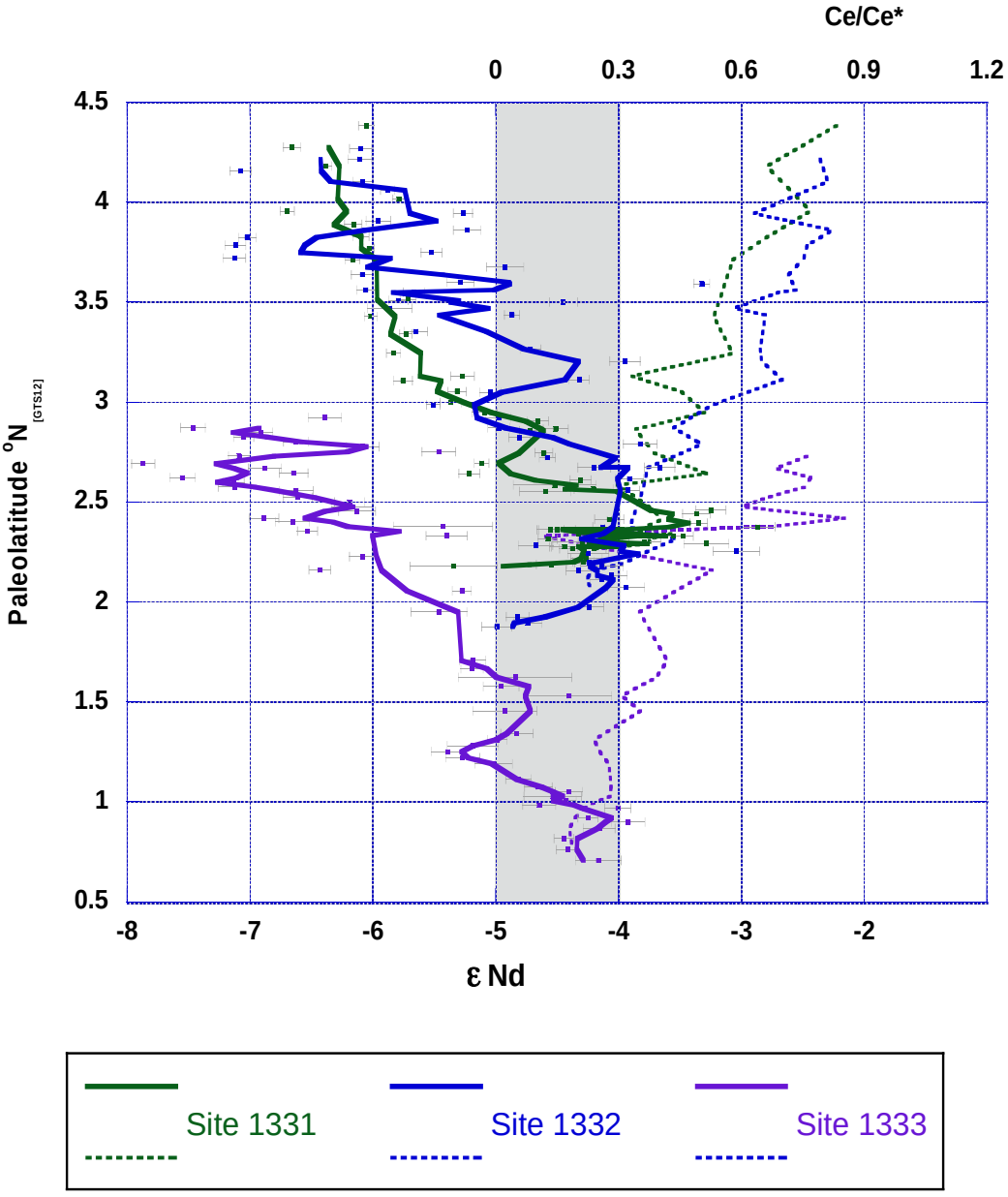

Figure 4.1. ε_{Nd} values with 3 pt. smoothed line and Ce/Ce* anomaly plotted against paleolatitudes for each sample, calculated from interpolated paleolocations from (Palike et. al., 2012) using sample ages calculated from GTS 2012 age model (Westerhold et. al., 2013). Gray box delineates seawater conditions during period of interest from fossil fish teeth record from same sites (Scher, In Prep.)

CHAPTER 5

CONCLUSION

This study has documented temporal and spatial differences within the ODED fraction during times of differing thermal gradients through the middle Eocene to early Oligocene. The winds seem to temporally intensify delivering less radiogenic values indicative of older continental values not from the Americas and trend further away from geochemical seawater signatures as the thermal gradient increases. The cause of the biasing seawater signature may be attributed to sedimentary phase changes in the ODED due to the latitudinal position relative to the high productive zone and/or the depth of the CCD, providing temporal and spatial constraints on the ODED samples and extractions. Pivotally, due to the nature of the study and that of the operationally defined component, more work needs to be performed, like that of SEM and XRD measurements on the samples to make more conclusive, robust linkages, providing a better understanding of the conditions at hand. For that reason this study shows more so than anything the lack and the need for further investigation of atmospheric conditions throughout the history of the Earth.

REFERENCES

Abelson, M., Agnon, A., & Almogi-Labin, A. (2008). Indications for control of the Iceland plume on the Eocene–Oligocene “greenhouse–icehouse” climate transition. Earth and Planetary Science Letters, 265(1), 33-48.

Bailey, J.C., (1993). Geochemical history of sediments in the north-western Pacific Ocean, Geochem. J. 27 (2) 71–90.

Bayon, G., German, C. R., Boella, R. M., Milton, J. A., Taylor, R. N., & Nesbitt, R. W. (2002). An improved method for extracting marine sediment fractions and its application to Sr and Nd isotopic analysis. Chemical Geology, 187(3), 179-199.

Bayon, G., German, C. R., Burton, K. W., Nesbitt, R. W., & Rogers, N. (2004). Sedimentary Fe–Mn oxyhydroxides as paleoceanographic archives and the role of aeolian flux in regulating oceanic dissolved REE. Earth and Planetary Science Letters, 224(3), 477-492.

Bohaty, S. M., Zachos, J. C., Florindo, F., & Delaney, M. L. (2009). Coupled greenhouse warming and deep-sea acidification in the middle Eocene. Paleoceanography, 24(2), PA2207.

Bohaty, S. M., & Zachos, J. C. (2003). Significant Southern Ocean warming event in the late middle Eocene. Geology, 31(11), 1017-1020.

Chester, H., & Hughes, M.J. (1967). A chemical technique for the separation of ferromanganese minerals, carbonate minerals and adsorbed trace elements from pelagic sediments.Chem.Geol.2, 249~262.

Cramer, B. S., Toggweiler, J. R., Wright, J. D., Katz, M. E., & Miller, K. G., (2009). Ocean overturning since the Late Cretaceous: Inferences from a new benthic foraminiferal isotope compilation. Paleoceanography, 24(4).

Coxall, H. K., & P. A. Wilson, (2011). Early Oligocene glaciation and productivity in the eastern equatorial Pacific: Insights into global carbon cycling, Paleoceanography, 26, PA2221, doi:10.1029/2010PA002021.

Dore, J.E., Lukas, R., Sadler, D.W., and Karl, D.M., (2003). Climate-driven changes to the atmospheric CO2 sink in the subtropical North Pacific Ocean. Nature (London, U. K.).

Eisenhauer, A., Meyer, H., Rachold, V., Tütken, T., Wiegand, B., Hansen, B. T., ... & Kassens, H., (1999). Grain size separation and sediment mixing in Arctic Ocean sediments: evidence from the strontium isotope systematic. Chemical geology, 158(3), 173-188.

Elderfield,H. & Greaves, M.J., (1981). Negative Cerium anomalies in the rare earth element patters of oceanic ferromanganese nodules. Earth Planet. Sci. Lett. 55, 163-170.

Elderfield, H., Hawkesworth, C. J., Greaves, M. J., & Calvert, S. E., (1981). Rare earth element geochemistry of oceanic ferromanganese nodules and associated sediments. Geochimica et Cosmochimica Acta, 45(4), 513-528.

Feng, J. L., Zhu, L. P., Zhen, X. L., & Hu, Z. G., (2009). Grain size effect on Sr and Nd isotopic compositions in eolian dust: implications for tracing dust provenance and Nd model age. Geochemical Journal, 43(2), 123-131.

Goldberg, E.D., Arrhenius, G.O.S., (1958). Chemistry of Pacific pelagic sediments. Geochim. Cosmochim. Acta, 13, 153–212.

Grousset, F. E., & Biscaye, P. E., (2005). Tracing dust sources and transport patterns using Sr, Nd and Pb isotopes. Chemical Geology, 222(3), 149-167.

Heath, G. R., & Dymond, J., (1977). Genesis and transformation of metalliferous sediments from the East Pacific Rise, Bauer Deep, and Central Basin, northwest Nazca plate. Geological Society of America Bulletin, 88(5), 723-733.

Houben, A. J., van Mourik, C. A., Montanari, A., Coccioni, R., & Brinkhuis, H., (2011). The Eocene–Oligocene transition: Changes in sea level, temperature or both?. Palaeogeography, Palaeoclimatology, Palaeoecology.

Hovan, S. A., (1995). 28. LATE CENOZOIC ATMOSPHERIC CIRCULATION INTENSITY AND CLIMATIC HISTORY RECORDED BY EOLIAN DEPOSITION IN THE EASTERN EQUATORIAL PACIFIC OCEAN, LEG 138.Proceedings of the Ocean Drilling Program, Scientific Results. Proceedings of the Ocean Drilling Program, Scientific Results, 615-625.

Hovan, S. A., & Rea, D. K., (1992). Paleocene/Eocene boundary changes in atmospheric and oceanic circulation: a Southern Hemisphere record. Geology, 20(1), 15-18.

Hyeong, K., Park, S.H., Yoo, C. M., & Kim, K.H., (2005). Mineralogical and geochemical compositions of the eolian dust from the northeast equatorial Pacific and their implications on paleolocation of the Intertropical Convergence Zone. Paleoceanography. 20, PA1010, doi: 10.1029/2004PA001053.

Jahn, B.M., S. Gallet, J.M. Han, (2001). Geochemistry of the Xining, Xifeng and Jixian sections, Loess Plateau of China: eolian dust provenance and paleosol evolution during the last 140 ka, Chem. Geol. 178 (1–4) 71–94.

Janecek, T. R., & Rea, D. K., (1983). Eolian deposition in the northeast Pacific Ocean: Cenozoic history of atmospheric circulation. Geological Society of America Bulletin, 94(6), 730-738.

Jones, C.E., Halliday, A.N., Rea, D.K., Owen, R.M., (2000). Eolian inputs of lead to the North Pacific. Geochim. Cosmochim. Acta, (64), 1405-1416.

Jovane, L., Coccioni, R., Marsili, A., & Acton, G., (2009). The late Eocene greenhouse-icehouse transition: Observations from the Massignano global stratotype section and point (GSSP). The Late Eocene Earth: Hothouse, Icehouse, and Impacts, Geological Society of America, Boulder, 149-168.

Koppers, A. A., Staudigel, H., Pringle, M. S., & Wijbrans, J. R., (2003). Short lived and discontinuous intraplate volcanism in the South Pacific: Hot spots or extensional volcanism?. Geochemistry, Geophysics, Geosystems, 4(10).

Kuroda, J., and Westerhold, T., (2013). Data report: volcanic glass shards from the Eocene–Oligocene transition interval at Site U1333. In Pälike, H., Lyle, M., Nishi, H., Raffi, I., Gamage, K., Klaus, A., and the Expedition 320/321 Scientists, Proc. IODP, 320/321: Tokyo (Integrated Ocean Drilling Program Management International, Inc.). doi:10.2204/iodp.proc. 320321.211.2013.

Lear, C. H., Bailey, T. R., Pearson, P. N., Coxall, H. K., & Rosenthal, Y., (2008). Cooling and ice growth across the Eocene-Oligocene transition. Geology, 36(3), 251-254.

Leduc, G., Vidal, L., Cartapanis, O., Bard, E., (2009). Modes of eastern equatorial Pacific thermocline variability: implications for ENSO dynamics over the last glacial period. Paleoceanography 24, PA3202.

Luo, C., Mahowald, N.M., del Corral, J., (2003). Sensitivity study of meteorological parameters on mineral aerosol mobilization, transport, and distribution. J. Geophys. Res. Atmos. 108.

Lyle, M., Olivarez Lyle, A., Backman, J., & Tripati, A., (2005). Biogenic sedimentation in the Eocene equatorial Pacific-the stuttering greenhouse and Eocene carbonate compensation depth. In Wilson, P.A., Lyle, M., & Firth, J.V. (Eds.), Proc. ODP, Sci. Results, 199, 1-35 [Online]. <http://www.odp.tamu.edu/publications/199_SR/VOLUME/CHAPTERS/219.PDF> [Cited 2014-07-20].

Lyle, M., (2003). Neogene carbonate burial in the Pacific Ocean. Paleoceanography, 18(3), 1059, doi:10.1029/2002PA000777.

Maher, B.A., Prospero, J.M., Mackie, D., Gaiero, D., Hesse, P.P., Balkanski, Y., (2010). Global connections between aeolian dust, climate and ocean biogeochemistry at the present day and at the last glacial maximum. Earth Sci. Rev. 99, 61–97.

McCulloch, M. T., & Wasserburg, G. J., (1978). Sm-Nd and Rb-Sr chronology of continental crust formation. Science, 200(4345), 1003-1011.

McGee, D., Marcantonio, F., & Lynch-Stieglitz, J., (2007). Deglacial changes in dust flux in the eastern equatorial Pacific. Earth and Planetary Science Letters,257(1), 215-230.

Miller, K. G., J. D. Wright, M. E. Katz, B. S. Wade, J. V. Browning, B. S. Cramer, and Y. Rosenthal, (2009). Climate threshold at the Eocene- Oligocene transition: Antarctic ice sheet influence on ocean circulation, Spec. Pap. Geol. Soc. Am., 452, 169–178, doi:10.1130/2009.245211.

Moebius, I., Friedrich, O., & Scher, H.D., (2014). Changes in Southern Ocean bottom water environments associated with the Middle Eocene Climatic Optimum. Palaeogeography, Palaeoclimatology, Palaeoecology, 405, 16-27.

Moore, N. T., Backman, J., Raffi, I., Nigrini, C., Sanfilippo, A., Pälike, H., & Lyle, M., (2004). Paleogene tropical Pacific: Clues to circulation, productivity, and plate motion. Paleoceanography, 19(3).

Moore Jr, T. C., Jarrard, R. D., Lyle, A. O., & Lyle, M., (2008). Eocene biogenic silica accumulation rates at the Pacific equatorial divergence zone. Paleoceanography, 23(2), PA2202.

Moore, Jr. T. C., Rea, D. K., Lyle, M., & Liberty, L. M., (2002). Equatorial ocean circulation in an extremely warm climate. Paleoceanography, 17(1), 5-1.

Nakai, S. I., Halliday, A. N., & Rea, D. K., (1993). Provenance of dust in the Pacific Ocean. Earth and Planetary Science Letters, 119(1), 143-157.

Olivarez Lyle, A., & M.W. Lyle, (2002). Determination of biogenic opal in pelagic marine sediments: a simple method revisited, in: M. Lyle, P.A. Wilson, T.R. Janecek, et al., (Eds.), Proc. Ocean Drill. Program, Init. Repts, vol. 199, Ocean Drilling Program, College Station, TX, (2002).

Olivarez, A. M., Owen, R. M., & Rea, D. K., (1991). Geochemistry of eolian dust in Pacific pelagic sediments: Implications for paleoclimatic interpretations. Geochim. Cosmochim. Acta, (55). 2147-2158.

Palike, H., Norris, R.D., Herrle, J.O., Wilson, P.A., Coxall, H.K., Lear, C.H., Shackleton, N.J., Tripati, A.K., Wade, B.S., (2006). The Heatbeat of the Oligocene Climate System, Science 314 (5807). 1894-1898, doi:10.1126/science.1133822.

Palike, H., Lyle, M., Nishi, H., Raffi, I., Gamage, K., Klaus, A., & the Expedition 320/321 Scientists, (2010). Proceedings of the Integrated Ocean Drilling Program (IODP). v. 320/321. Tokyo, Integrated Ocean Drilling Program Management International, Inc., doi: 10.2204/iodp.proc.320321.2010.

Pälike, H., Lyle, M. W., Nishi, H., Raffi, I., Ridgwell, A., Gamage, K., ... & Sawada, K., (2012). A Cenozoic record of the equatorial Pacific carbonate compensation depth. Nature, 488(7413), 609-614.

Pearson, P. N., G. L. Foster, and B. S. Wade, (2009). Atmospheric carbon dioxide through the Eocene-Oligocene climate transition, Nature, 461, 1110–1113, doi:10.1038/nature08447.

Pettke, T., Halliday, A. N., Hall, C. M., & Rea, D. K., (2000). Dust production and deposition in Asia and the north Pacific Ocean over the past 12 Myr. Earth and Planetary Science Letters, 178(3), 397-413.

Pettke, T., Halliday, A. N., & Rea, D. K., (2002). Cenozoic evolution of Asian climate and sources of Pacific seawater Pb and Nd derived from eolian dust of sediment core LL44-GPC3. Paleoceanography, 17(3), 3-1.

Plank, T., & Langmuir, C. H., (1998). The chemical composition of subducting sediment and its consequences for the crust and mantle. Chemical Geology, 145(3), 325-394.

Rea, D. K., & Lyle, M. W., (2005). Paleogene calcite compensation depth in the eastern subtropical Pacific: Answers and questions. Paleoceanography, 20(1).

Rea, D. K., Moore Jr, T. C., & Lyle, M., (2000). Atmospheric and oceanic circulation dynamics in the equatorial Pacific of the Paleogene world. GFF, 122(1), 135-136.

Rea, D. K. (1994). The paleoclimatic record provided by eolian deposition in the deep sea: The geologic history of wind. Reviews of Geophysics, 32(2), 159-195.

Rea, D. K., Leinen, M., & Janecek T.R., (1985). A geologic approach to the long-term history of atmospheric circulation. Science 227, 721-725.

Rea, D. K., & Janecek, T. R., (1982). Late Cenozoic changes in atmospheric circulation deduced from North Pacific eolian sediments. Marine Geology, 49(1), 149-167.

Rea, D. K., & Janecek, T. R., (1981). Mass-accumulation rates of the non-authigenic inorganic crystalline (eolian) component of deep-sea sediments from the western Mid-Pacific Mountains, Deep Sea Drilling Project Site 463. Initial Reports of the Deep Sea Drilling Project, 62, 653-659.

Scher, H. D., S. M. Bohaty, B. W. Smith, & G. H. Munn, (2014). Isotopic interrogation of a suspected late Eocene glaciation, Paleoceanography, 29, doi:10.1002/2014PA002648.

Scher, H. D., & Delaney, M. L., (2010). Breaking the glass ceiling for high resolution Nd isotope records in early Cenozoic paleoceanography. Chemical Geology, 269(3), 329-338.

Scher, H. D., & E. E. Martin, (2008). Oligocene deep water export from the North Atlantic and the development of the Antarctic Circumpolar Current examined with neodymium isotopes, Paleoceanography, 23, PA1205, doi:10.1029/2006PA001400.

Scher, H. D., & E. E. Martin, (2006). Timing and climatic consequences of the opening of Drake Passage, Science, 312, 428–430, doi:10.1126/science.1120044.

Severmann, S., R.A. Mills, M.R. Palmer, A.E. Fallick., (2004). The origin of clay minerals in active and relict hydrothermal deposits, Geochim. Cosmochim. Acta, 68(1), 73–88.

Stancin, A. M., Gleason, J. D., Rea, D. K., Owen, R. M., Moore Jr, T. C., Blum, J. D., & Hovan, S. A., (2006). Radiogenic isotopic mapping of late Cenozoic eolian and hemipelagic sediment distribution in the east-central Pacific. Earth and Planetary Science Letters, 248(3), 840-850.

Takebe, M., (2005). Carriers of Rare Earth Elements in Pacific Deep Sea Sediments. The Journal of geology, 113(2), 201-215.

Taylor, S. R., and S. M. McClennan, (1985). The Continental Crust: Its Composition and Evolution, 312 pp., Blackwell Sci., Malden, Mass.

Toyoda, K., & A. Masuda, (1991). Chemical leaching of pelagic sediments: identification of the carrier of Ce anomaly, Geochem. J., 25(2), 95–119.

Toyoda, K., Nakamura, Y., and Masuda, A., (1990). Rare earth elements of Pacific pelagic sediments. Geochim. Cosmochim. Acta, 54,1033-1103.

Westerhold, T., Röhl, U., Pälike, H., Wilkens, R., Wilson, P. A., & Acton, G., (2013). Orbitally tuned time scale and astronomical forcing in the middle Eocene to early Oligocene. Climate of the Past Discussions, 9(6), 6635-6682.

Winckler, G., Anderson, R. F., Fleisher, M. Q., McGee, D., & Mahowald, N., (2008). Covariant glacial-interglacial dust fluxes in the equatorial Pacific and Antarctica. Science, 320(5872), 93-96.

Xie, R. C., & Marcantonio, F., (2012). Deglacial dust provenance changes in the Eastern Equatorial Pacific and implications for ITCZ movement. Earth and Planetary Science Letters, 317, 386-395.

Ziegler, C. L., Murray, R. W., Hovan, S. A., & Rea, D. K., (2007). Resolving eolian, volcanogenic, and authigenic components in pelagic sediment from the Pacific Ocean. Earth and Planetary Science Letters, 254(3), 416-432.

Zachos, J. C., Dickens, G. R., & Zeebe, R. E., (2008). An early Cenozoic perspective on greenhouse warming and carbon-cycle dynamics. Nature, 451(7176), 279-283.

Zachos, J., Pagani, M., Sloan, L., Thomas, E., & Billups, K., (2001). Trends, rhythms, and aberrations in global climate 65 Ma to present. Science, 292(5517), 686-693.